Heterotypic interactions in the dilute phase can drive co-condensation of prion-like low-complexity domains of FET proteins and mammalian SWI/SNF complex

Authors: Richoo B. Davis[1], Anushka Supakar[2], Aishwarya Kanchi Ranganath[3], Mahdi Muhammad Moosa[1], Priya R. Banerjee[1, 2,3] *

Affiliations:
[1]Department of Physics, University at Buffalo, Buffalo NY 14260, USA
[2]Department of Biological Sciences, University at Buffalo, Buffalo NY 14260, USA
[3]Department of Chemical and Biological Engineering, University at Buffalo, Buffalo NY 14260, USA

*Corresponding author: P. R. B.; prbanerj@buffalo.edu

Abstract

Prion-like domains (PLDs) are low-complexity protein sequences enriched within nucleic acid-binding proteins including those involved in transcription and RNA processing. PLDs of FUS and EWSR1 play key roles in recruiting chromatin remodeler mammalian SWI/SNF complex to oncogenic FET fusion protein condensates. Here, we show that disordered low-complexity domains of multiple SWI/SNF subunits are prion-like with a strong propensity to undergo intracellular phase separation. These PLDs engage in sequence-specific heterotypic interactions with the PLD of FUS in the dilute phase at sub-saturation conditions, leading to the formation of PLD co-condensates. In the dense phase, homotypic and heterotypic PLD interactions are highly cooperative, resulting in the co-mixing of individual PLD phases and forming spatially homogeneous co-condensates. Heterotypic PLD-mediated positive cooperativity in protein-protein interaction networks is likely to play key roles in the co-phase separation of mSWI/SNF complex with transcription factors containing homologous low-complexity domains.

Introduction

Biomolecular condensates such as stress granules and transcription factories are membrane-less subcellular bodies that form and are regulated via the phase separation of multivalent proteins and nucleic acids [1–3]. The physiological functions of biomolecular condensates range from signaling hubs under normal conditions to storage depots in response to cellular stress [3]. Sequence analyses of the proteins enriched in intracellular condensates both in the nucleus and cytoplasm have previously revealed an abundance of proteins containing long stretches of intrinsically disordered prion-like domains [4,5]. Prion-like domains (PLDs) are typically characterized by their low complexity sequence features with an overrepresentation of aromatic (Y/F) and polar amino acids (G/S/Q/N) and depletion of charged residues [6,7]. Proteins with PLDs have been identified in all life forms [8–12]. Prion proteins were initially discovered as proteinaceous infectious agents in bovine spongiform encephalopathy and other neurodegenerative diseases [4,13–15], but are increasingly recognized with key functional roles in driving phase separation of RNA-binding proteins in the cell, and in the formation of functional amyloids [16,17].

What roles do PLDs play in the context of protein phase separation? Multivalent cohesive interactions between PLD chains as well as the chain-solvent interactions, which are encoded by the PLD primary sequence composition and patterning [18,19], have been recognized to be a key feature driving the phase separation of isolated PLD chains and PLD-containing proteins [20–25]. Previous studies using hnRNP A1 PLD have demonstrated that the distributed aromatic (Y/F) amino acids act as “stickers” that mediate PLD-PLD interactions [18,26], whereas the polar amino acids (S/G) can be described as “spacers”, which regulate chain solvation and cooperativity of sticker-sticker interactions. The importance of tyrosine residues in driving PLD phase separation has been further demonstrated experimentally for FUS [26] and EWSR1 [27], and computationally for a large number of PLD sequence variants [28]. In addition to aromatic residues, charged residues such as arginine (R) and polar amino acids such as glutamine (Q) also play smaller but important roles in PLD phase separation [28]. Together, the sticker and spacer residues regulate PLD phase separation in a context-dependent manner [19]. In a broader context, however, the sequence grammar encoding LCD phase separation can be more complex and additional factors beyond aromaticity, such as the net charge and hydrophobicity of LCDs are likely to play equally dominant roles in their phase separation [29,30]. When part of a multi-domain protein, π-π and cation-π interactions mediated by the aromatic and arginine residues in PLDs have been shown to drive phase separation of many full-length RNA and DNA binding proteins including FUS, EWSR1, TAF15, hnRNP A1, and EBF1 [21,31–33]. Further, debilitating point mutations in PLDs have been reported to promote the pathological transformation of protein condensates from a liquid-like state to solid aggregates [20,34,35]. Thus, PLDs play important roles in the context of functional protein phase separation as well as disease processes associated with the formation of aberrant biomolecular condensates.

Many intracellular biomolecular condensates, such as stress granules and transcriptional hubs, are known to contain a multitude of proteins containing prion-like LCDs [4,36,37]. Despite being broadly classified as prion-like based on the frequencies of certain amino acids in a protein sequence, as noted above [6,7], individual PLD chains typically feature distinct sequence composition, amino acid patterning, and chain length [4,22,38]. Do PLDs from distinct yet functionally related proteins interact with one another and undergo co-phase separation? Previous studies have reported that the PLDs in transcription factors, including the FET family of fusion

oncoproteins, not only drive their phase separation but also facilitate the recruitment of essential coactivators, such as the catalytic subunit of the mammalian SWI/SNF complex, BRG1, in transcriptional condensates [32,39–42]. Interestingly, BRG1 contains an N-terminal LCD that is prion-like, which can engage with the PLDs of FET fusion proteins via heterotypic interactions [32]. Although homotypic phase separation of some PLDs, such as FUS and hnRNP A1, are well characterized [18,19,31], little is known about how heterotypic interactions regulate the co-phase separation of PLD mixtures [36] and how the sequence features of respective PLD chains contribute to this process. In general, in multi-component mixtures of multivalent LCDs, homotypic and heterotypic interactions between LCD chains can either positively cooperate, negatively cooperate, or form coexisting phases, resulting in a diverse phase behavior and dense phase co-partitioning. The interplay between the specificity and strengths of homotypic and heterotypic interactions dictates the co-condensation versus discrete condensate formation in an LCD sequence-specific manner [43]. Further, PLD-containing proteins such as FUS have recently been reported to form a heterogeneous pool of oligomeric complexes below their saturation concentration for phase separation [44], which are thought to represent distinct functional states of the protein than the condensates that form at higher concentrations [45]. However, a key unanswered question is whether heterotypic PLD interactions occur at sub-saturation conditions, which may provide a mechanism for LCD-mediated functional protein recruitments such as interactions between FET oncofusions and mSWI/SNF complex in the absence of phase separation underlying oncogenic transcriptional programs.

Motivated by these open questions, here we systematically investigate the phase behavior of PLD mixtures encompassing FUS^{PLD} and the PLDs from the chromatin remodeler mammalian SWI/SNF (mSWI/SNF) complex that aberrantly interact with FUS fusion oncoproteins in transcriptional reprogramming [46]. Our study incorporates PLDs from four mSWI/SNF complex subunits: ARID1A, ARID1B, SS18, and BRG1, which are essential components for spatiotemporal transcriptional regulation and chromatin remodeling [47–49]. Employing in vitro experiments in conjunction with mammalian cell culture models, we show that there exists a broad range of saturation concentrations (C_{sat}) of PLD chains in vitro that directly correlate with their ability to form phase-separated condensates in live cells. We find that, except BRG1, mSWI/SNF subunit PLDs undergo phase separation with C_{sat} values substantially lower than the known PLDs of RNA-binding proteins such as TAF15, EWSR1, and FUS [18,31], suggesting a greater degree of homotypic interactions. Similar to FET PLDs, the phase separation propensity of mSWI/SNF PLDs is primarily dependent on aromatic residues, specifically tyrosine residues, and to a smaller extent on polar amino acids such as glutamine. Despite strong homotypic interactions, mSWI/SNF PLDs engage in heterotypic PLD interactions with FUS^{PLD}, resulting in co-partitioning in the dense phase with partition coefficients that show a positive correlation with the number of aromatic residues. In mixtures of PLD condensates, individual PLD phases undergo complete mixing, and together, they form spatially homogeneous PLD co-condensates. These findings indicate that homotypic and heterotypic PLD interactions act cooperatively in the dense phase despite substantially different saturation concentrations of individual PLD chains, which we posit to be a direct manifestation of similarity in PLD sequence grammars. Importantly, heterotypic PLD-PLD interactions between FUS and mSWI/SNF subunits are detectable at sub-saturation concentrations in vitro and in live cells, indicating strong affinities between these low-complexity domains in the absence of phase separation. The observed specificity in interactions among PLDs

is further highlighted by a lack of interactions between these PLDs with a functionally distinct non-prion-like LCD of a transcriptional repressor protein. We conjecture that PLD-mediated selective co-condensation of multiple subunits of the mSWI/SNF chromatin remodeling complex with FET fusion proteins may constitute an important step in establishing transcriptionally relevant protein interaction networks.

Results

Prion-like domains of mSWI/SNF subunits form dynamic phase-separated condensates in live cells

mSWI/SNF chromatin remodeler complex is enriched in subunits that have large disordered low complexity regions with unknown functions [50]. Many of these disordered regions have prion-like sequences (**Fig. S1**) [32]. Since PLDs of RNA and DNA binding proteins can drive phase separation and contribute to the formation of biomolecular condensates in cells [4,21,31], we investigated whether mSWI/SNF subunit PLDs are phase separation competent. We selected the top four PLDs in the complex based on their length, functional and disease relevance, which correspond to the following subunits - BRG1 [catalytic subunit], ARID1A, and ARID1B [among most mutated proteins in cancer [49]], and SS18 [relevant to fusion oncoprotein SS18-SSX [51]] (**Figs. 1a,b; S1**). We noted that although the prion prediction algorithm PLAAC [6] categorizes these low complexity domains as prion-like, these PLDs have varying sequence composition and their lengths are significantly higher than the PLDs from RNA binding proteins (**Fig. 1b**; **Tables S1-3**). To determine if they were phase separation competent, we titrated concentrations of recombinant PLDs in vitro (buffer: 125mM NaCl, 25mM Tris.HCl pH 7.5) and observed that apart from BRG1^{PLD}, all other PLDs form spherical condensates in a concentration-dependent manner (**Figs. 1c; S2a**). Further, ARID1B^{PLD} condensates showed cluster-like morphologies upon phase separation, suggesting a percolation-type network formation [52] (**Fig. 1c**). Based on the optical microscopy data, we quantified the saturation concentrations (C_{sat}) for the PLDs as $\leq$ 2.5 μM for ARID1A^{PLD} and SS18^{PLD}, and $\leq$ 5 μM for ARID1B^{PLD} (**Fig. 1d; S2a**). Under similar experimental conditions, FUS^{PLD} undergoes phase separation with a C_{sat} of $\leq$ 200 μM (**Fig. S2a**) [53], which is almost two orders of magnitude higher than ARID1A^{PLD} and SS18^{PLD}. Although BRG1^{PLD} did not phase separate under these conditions (**Fig. S2a**) it can be induced to form spherical condensates in the presence of a macromolecular crowder (20% Ficoll PM70; **Fig. S2b**) [32]. These data suggest that except for BRG1, mSWI/SNF subunit PLDs are highly phase separation competent. We next probed whether these condensates are dynamic using fluorescence recovery after photobleaching (FRAP) experiments. FRAP recovery traces indicate that all PLD condensates have liquid-like properties with varying diffusivity dynamics. (**Fig. 1e**). Based on the FRAP traces, we find that ARID1A^{PLD} forms the most dynamic condensates with more than 80% recovery, SS18^{PLD} is intermediate with ~60% recovery, and ARID1B^{PLD} is the least dynamic with less than 40% recovery within the same observational timeframe. The reduced dynamicity of ARID1B^{PLD} condensates is consistent with the percolation-driven network formation observed for these condensates (**Fig. 1c**).

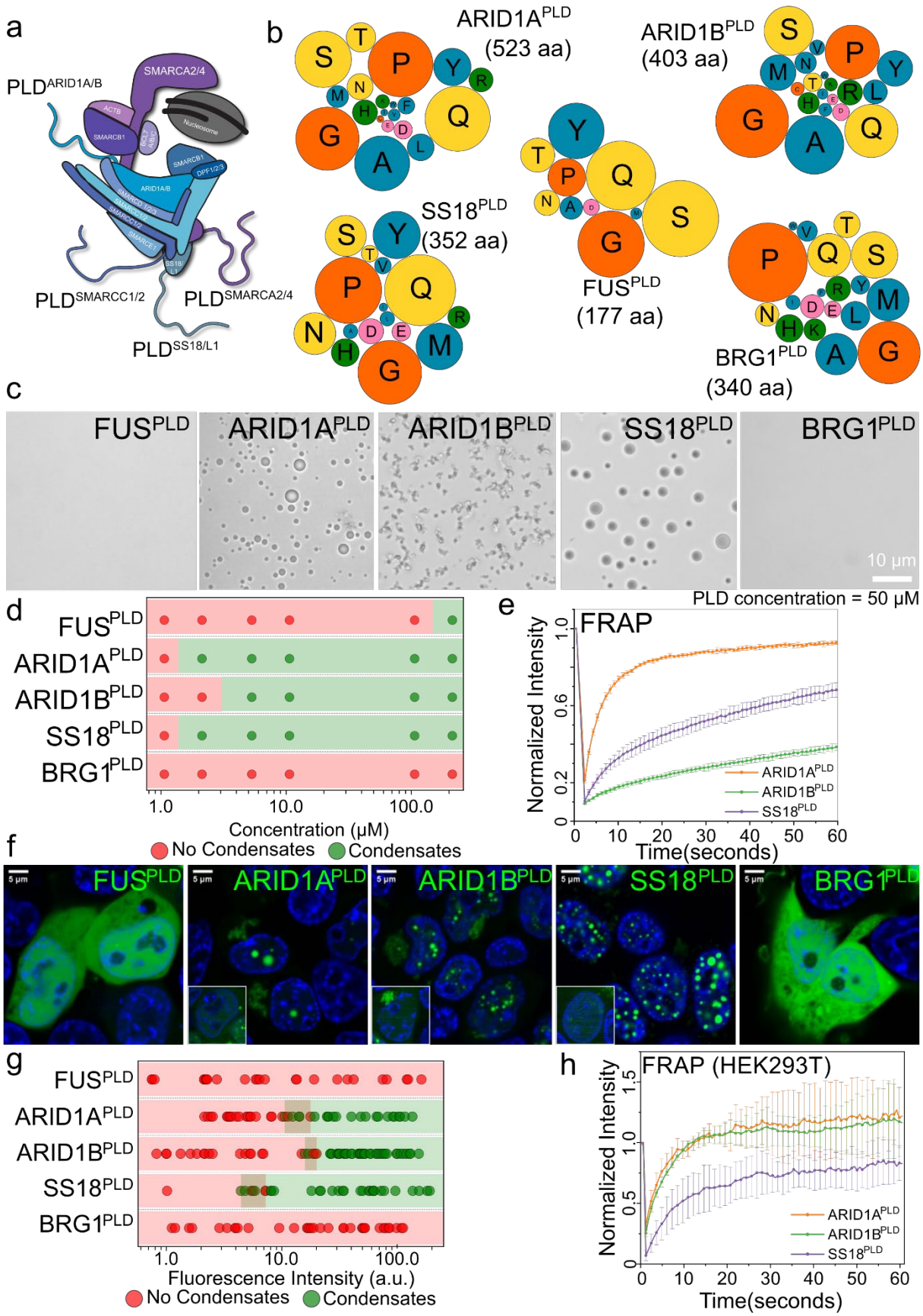
a
PLD^ARID1A/B
SMARCA2/4
ACTB
SMARCB1
Nucleosome
SMARCB1
DPF1/2/3
ARID1A/B
SMARCC1/2
SMARCE1
SS18/L1
PLD^SMARCC1/2
PLD^SMARCA2/4
PLD^SS18/L1
b
ARID1A^PLD (523 aa)
ARID1B^PLD (403 aa)
SS18^PLD (352 aa)
FUS^PLD (177 aa)
BRG1^PLD (340 aa)
c
FUS^PLD
ARID1A^PLD
ARID1B^PLD
SS18^PLD
BRG1^PLD
10 µm
d
FUS^PLD
ARID1A^PLD
ARID1B^PLD
SS18^PLD
BRG1^PLD
1.0
10.0
100.0
Concentration (µM)
No Condensates
Condensates
e
PLD concentration = 50 µM
FRAP
Normalized Intensity
Time(seconds)
ARID1A^PLD
ARID1B^PLD
SS18^PLD
f
5 µm
FUS^PLD
ARID1A^PLD
ARID1B^PLD
SS18^PLD
BRG1^PLD
g
FUS^PLD
ARID1A^PLD
ARID1B^PLD
SS18^PLD
BRG1^PLD
1.0
10.0
100.0
Fluorescence Intensity (a.u.)
No Condensates
Condensates
h
FRAP (HEK293T)
Normalized Intensity
Time(seconds)
ARID1A^PLD
ARID1B^PLD
SS18^PLD

Figure 1: Prion-like domains of mSWI/SNF complex subunits form phase-separated condensates in vitro and in live cells. **a)** A schematic of the mSWI/SNF complex bound to the nucleosome. This is adapted from Varga et al., BST, 2021 [54]. The four largest prion-like domains (PLDs) in the mSWI/SNF complex are displayed as shaded lines**. b)** A bubble chart representation of the sequence composition of the five PLDs (FUS, ARID1A, ARID1B, SS18, and BRG1) used in this study. The lengths of the PLDs are displayed as amino acid count "aa". The color codes for amino acids are provided in Table S6. **c)** Differential interference contrast (DIC) microscopy images of purified FUS^{PLD} and mSWI/SNF PLDs at 50 μM protein concentration. **d)** Concentration titrations of various PLDs are displayed as state diagrams with green circles denoting the two-phase regime and red circles denoting the single-phase regime (*see* DIC images in **Fig. S2**). **e)** Fluorescence recovery after photobleaching (FRAP) curves for condensates formed by $ARID1A^{PLD}$, $ARID1B^{PLD}$, and $SS18^{PLD}$ at 50 μM concentrations. The FRAP curves show the average intensity and standard deviation of the intensity profiles as a function of time (n ≥ 3). **f)** Fluorescence microscopy images of HEK293T cells expressing GFP-tagged PLDs (FUS^{PLD}, $ARID1A^{PLD}$, $ARID1B^{PLD}$, $SS18^{PLD}$ and $BRG1^{PLD}$), as indicated. Hoechst was used to stain the cell nucleus, which is shown in blue. The insets show images of cells expressing GFP-tagged proteins below their respective saturation concentrations. **g)** The relative phase separation capacities were quantified from the fluorescence intensity of intracellularly expressed GFP-tagged proteins (a proxy for protein concentration) and presented as a state diagram. Green circles indicate the presence of nuclear condensates and red circles represent diffused expression patterns. The dark-shaded regions represent the transition concentrations (n = total of 30-60 cells from two replicates). **h)** FRAP curves for condensates formed by GFP-tagged PLDs in HEK293T cells. The average intensity and standard deviation of the intensity profiles are shown over time (n = 3). The scale bar is 5 μm for all images.

Although PLDs have emerged as a driver of many ribonucleoprotein phase separation under physiological and pathological conditions, expression of these domains alone typically does not lead to the formation of condensates in live cells [20,32,43,55]. This is consistent with their known C_{sat} values in vitro, which range from 100-200 μM and are typically much higher than their intracellular concentrations [18,31,53,56]. Since mSWI/SNF PLDs show low micromolar C_{sat} values in vitro, we posited that they may form condensates in live cells at relatively low expression levels compared to FUS^{PLD}. To test this idea, we transiently transfected HEK293T cells with GFP-PLD plasmids. Upon expression, $ARID1A^{PLD}$, $ARID1B^{PLD}$, and $SS18^{PLD}$ readily formed spherical nuclear foci, whereas $BRG1^{PLD}$ and FUS^{PLD} remained diffused at all expression levels (**Fig. 1f**). To estimate the relative C_{sat} of mSWI/SNF PLDs within the nucleus, we used GFP fluorescence intensity as a proxy for concentration and leveraged the stochastic nature of intracellular PLD expression that spanned over two orders of magnitude. We observed that $SS18^{PLD}$ has the lowest C_{sat} followed by $ARID1A^{PLD}$ and $ARID1B^{PLD}$ (**Figs. 1g; S4**). This rank order of cellular saturation concentrations is similar to their in vitro phase behavior (**Fig. 1d**). FRAP experiments revealed that the nuclear condensates of $ARID1A^{PLD}$, $ARID1B^{PLD}$, and $SS18^{PLD}$ are dynamic (**Fig. 1h**). Interestingly, the morphology of the PLD condensates varied with their subcellular localization. Spherical condensates formed within the nucleus and irregular, yet dynamic, assemblies were observed in the cytoplasm (**Figs. S2c,d**). Such differences could arise from the distinct intracellular microenvironment of the cytoplasm and the nucleus, such as the viscoelasticity of chromatin fibers, altered post-translational modifications, and high abundance of RNAs in the nucleus, which can markedly influence the coarsening behavior and biophysical properties of condensates [57–61].

Tyrosine residues play a dominant role in mSWI/SNF subunit PLD phase separation

The phase separation capacity of PLDs from RNA-binding proteins has been attributed to multivalent interactions predominantly mediated by the distributed aromatic and arginine residues

[61,62]. While SS18^{PLD} has a lower fraction of aromatic and arginine residues (0.11) than FUS^{PLD} (0.14; **Tables S1-3**), it possesses a greater number of aromatic and arginine residues (39) than FUS^{PLD} (24). To test if increasing the number of aromatic residues can improve the phase separation driving force of FUS^{PLD} without changing the overall sequence composition, we created a dimer of FUS^{PLD}, termed FUS^{2XPLD} (**Fig. 2a**), which possesses a total of 48 aromatic residues at a fixed fraction of 0.14. In contrast to the FUS^{PLD}, which remained diffused at all expression levels, we observed that FUS^{2XPLD} formed phase-separated condensates in the cell nucleus at a relatively low expression level (**Fig. 2b**) similar to the three mSWI/SNF subunit PLDs (**Fig. 1f**). The estimated intracellular saturation concentration of FUS^{2XPLD} was observed to be similar to that of ARID1A^{PLD}, ARID1B^{PLD}, and SS18^{PLD} (**Figs. 2b; S3a, S4**). Analogous to mSWI/SNF subunit PLD condensates, FRAP experiments revealed that FUS^{2XPLD} condensates have a high degree of dynamic behavior (**Fig. S3b**). To test whether the stronger driving force for phase separation of FUS^{2XPLD} primarily stems from the greater number of tyrosine residues and not simply from its increased length, we further created a variant of FUS^{2XPLD}, termed FUS$^{2XPLD\ halfYtoS}$, where we replaced the tyrosine residues to serine in the second half of the FUS^{2XPLD} (**Table S4**). This sequence variation led to a complete loss of phase separation FUS^{2XPLD} in living cells even at 10-fold higher intracellular concentrations (**Figs. 2a,b; S4**), implying that the number of tyrosine residues is a key determinant of phase separation in this PLD. Next, to test if tyrosine residues are also important for the phase separation of mSWI/SNF subunit PLDs, we first created an ARID1A^{PLD} variant where we mutated all 29 tyrosine residues to serine (29Y-to-S), termed ARID1A$^{PLD\ YtoS}$. We observed that 29Y-to-S substitution abolished the ARID1A^{PLD} phase separation in the cell at all expression levels (**Figs. 2c; S4**). Apart from tyrosine residues, ARID1A^{PLD} primary sequence shows enrichment of glutamines in the C-terminal region with multiple polyQ tracts with stretches of three to four Gln residues (**Table S4**). Previous studies have suggested that polyQ regions can promote LCD self-association [62,63]. However, when we mutated these Gln residues to Gly and created an ARID1A^{PLD} variant, termed ARID1A$^{PLD\ 30QtoG}$, we observed only a modest (~2 fold) increase intracellular C_{sat} (**Figs. 2c; S4**). These data suggest that Tyr residues play a greater role in driving homotypic ARID1A^{PLD} phase separation, similar to the FUS^{PLD}, whereas polar residues such as Gln play a moderate role.

Based on the results obtained from the sequence perturbations of FUS^{2XPLD} and ARID1A^{PLD}, it appears that intracellular phase separation of PLDs can be tuned by the number of Tyr residues. Since BRG1^{PLD}, which only contains seven aromatic residues but a large number of proline residues, does not phase separate in cells, we attempted to improve its condensation driving force by increasing the tyrosine content. To this end, we created two variants where we mutated 17 proline and 41 proline residues to tyrosine residues, termed BRG1$^{PLD\ Aro+}$ and BRG1$^{PLD\ Aro++}$, respectively. We observed that both BRG1^{PLD} variants can form intracellular condensates with comparable C_{sat} to other mSWI/SNF PLDs. However, the BRG1$^{PLD\ Aro++}$ was observed to form large irregular aggregates in the cytoplasm and was predominantly excluded from the nucleus (**Figs. 2d; S4**), which is likely due to strong homotypic interactions mediated by a large number of Tyr residues in this synthetic BRG1^{PLD} variant.

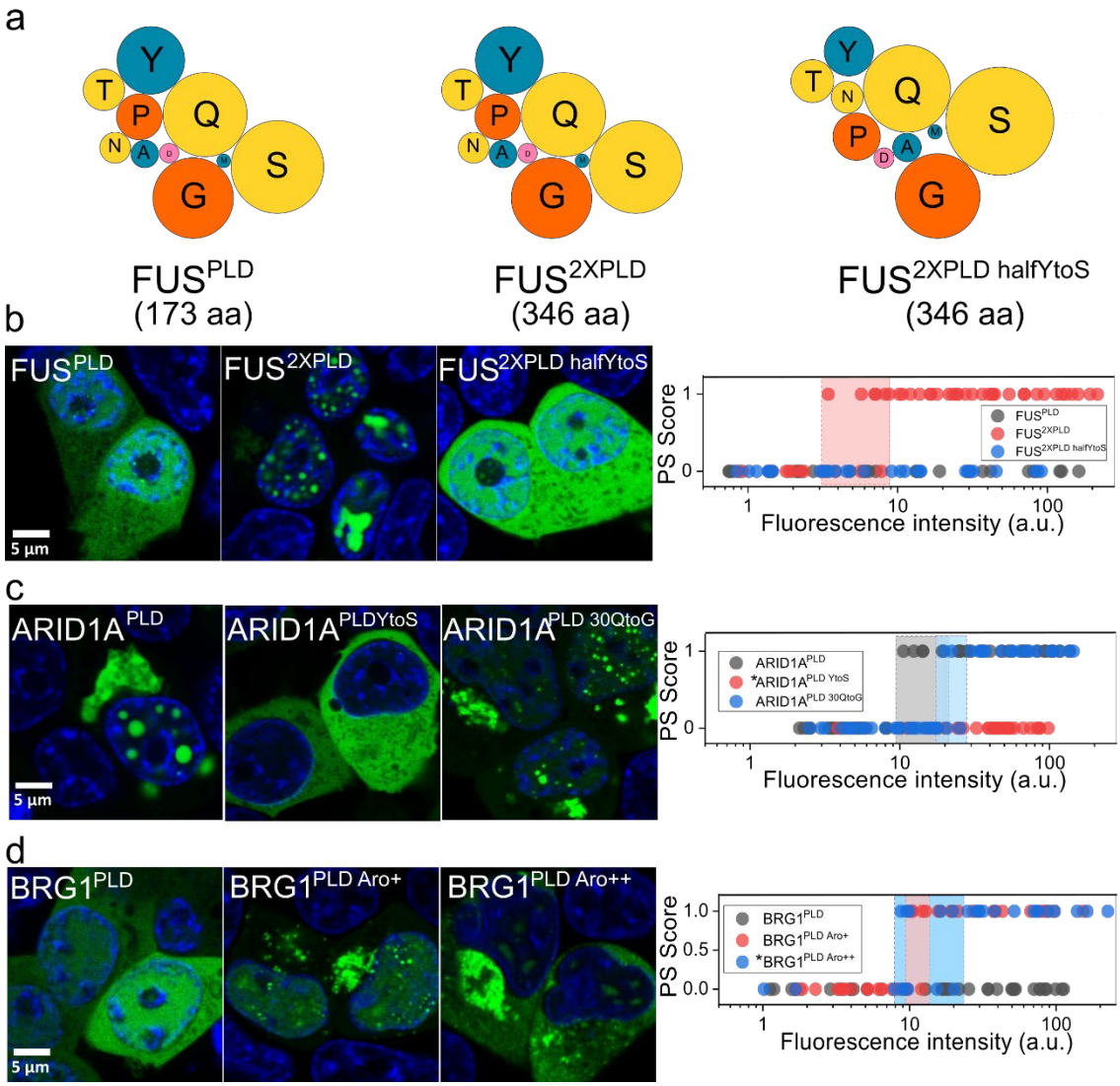

Figure 2: Tyrosine residues play a dominant role in mSWI/SNF PLD phase separation. a) A bubble chart representation of the sequence composition of FUS^{PLD}, FUS^{2XPLD}, and $FUS^{2XPLD\ half\ YtoS}$. The lengths of the PLDs are displayed as amino acid count "aa". Fluorescence microscopy images of HEK293T cells expressing GFP-tagged PLDs and variants of **b)** FUS^{PLD} (FUS^{PLD}, FUS^{2XPLD}, or $FUS^{2XPLD\ half\ YtoS}$), **c)** $ARID1A^{PLD}$ ($ARID1A^{PLD}$, $ARID1A^{PLD\ YtoS}$ and $ARID1A^{PLD\ 30QtoG}$), and **d)** $BRG1^{PLD}$ ($BRG1^{PLD}$, $BRG1^{PLD\ Aro+}$ and $BRG1^{PLD\ Aro++}$) as indicated. Hoechst was used to stain the cell nucleus, which is shown in blue. The phase separation capacity is quantified over various levels of nuclear protein concentrations. A phase separation (PS) score of '1' indicates the presence of nuclear condensates and a PS score of '0' represents diffused expression patterns. The shaded regions represent the transition concentrations. Asterisk '*' denotes cytoplasmic concentration. (n = total of 28-55 cells from two replicates). Also see **Fig. S4**.

mSWI/SNF PLD condensates recruit low-complexity domains of transcriptional machinery and RNA polymerase II via heterotypic interactions

An emerging feature underlying transcriptional regulation by prion-like low complexity domains in transcription factors is their ability to directly engage with chromatin remodeler SWI/SNF complexes [40,41,46] and RNA polymerase II (RNA pol II) [25], the carboxy-terminal domain (CTD) of which also has a prion-like sequence (**Fig. S5**). Our previous studies have reported that BRG1, the catalytic subunit of the mSWI/SNF complex, can enrich within optogenetically induced FUS^{PLD} condensates and FUS fusion protein condensates in live cells [63–65]. We posited that this functional engagement can be, in part, mediated by disordered PLDs of FUS and BRG1. Indeed, FUS^{2XPLD} condensates showed a strong colocalization with $BRG1^{PLD}$ in live cells (**Fig. S6**), which otherwise remains homogeneously distributed in the nucleus (**Fig. 1f**). This observation of $BRG1^{PLD}$ partitioning into FUS^{2XPLD} condensates suggests the occurrence of heterotypic PLD-PLD interactions in these systems. To explore these heterotypic interactions systematically, we analyzed the degree of the partitioning of PLDs of FUS and RNA pol II (**Table S4**) into condensates formed by $ARID1A^{PLD}$, $ARID1B^{PLD,}$ and $SS18^{PLD}$. To this end, we defined scaffolds and clients in each pair of PLD mixtures: scaffold is the protein that forms condensates ($C > C_{\mathrm{sat}}$) and the client, defined as the protein that does not homotypically phase separate under the experimental conditions ($C < C_{\mathrm{sat}}$), partitions into the scaffold condensates (**Fig. 3a**). The degree of client partitioning is determined by the sequence-specific scaffold-client interactions and the chain solvation free energy difference between the dense phase and the dilute phase [64–66]. When the experimental conditions are the same and the scaffold concentration is fixed, partition coefficients, defined as $k = {I_{dense}}/{I_{dilute}}$, of a group of similar clients to a scaffold condensate can report on the relative strength of scaffold-client interactions [64,65]. In our experiments, we observe that each of the PLD condensates can recruit other PLDs (**Figs. 3b; S7**), indicating a synergistic interplay between homotypic and heterotypic PLD interactions. However, the distribution of k values (**Fig. 3c**) spans over two orders of magnitude (~2−200), suggesting that there is a broad range of specificity of heterotypic interactions. We observed a few common trends for all three scaffold condensates: $SS18^{PLD}$, $ARID1A^{PLD}$, and $ARID1B^{PLD}$. Firstly, the partitioning of three strongly phase-separating mSWI/SNF PLDs within each other's condensates are similar and comparable to their self-partitioning (k ~ 50−220), suggesting that the sequence grammar driving homotypic PLD interactions are similar to the heterotypic interactions between these PLDs that governs co-partitioning. Secondly, $BRG1^{PLD}$, which showed a substantially lower propensity of phase separation (weaker homotypic interactions) than the other PLDs, partitioning within mSWI/SNF PLD condensates is almost 15-100-fold lower (k ~ 2−5), suggesting substantially weaker heterotypic PLD interactions in this case. Interestingly, we observed that FUS^{PLD} co-partitioned in mSWI/SNF subunit PLD condensates to a similar degree as the $SS18^{PLD}$, $ARID1A^{PLD}$, and $ARID1B^{PLD}$, (k ~ 50−185) despite its C_{sat} being greater than an order of magnitude higher than mSWI/SNF subunit PLD condensates. These observations suggest highly favorable heterotypic interactions, likely due to a homology in the sequence grammar of these PLDs. Finally, the CTD of RNA Pol II was observed to partition within mSWI/SNF PLD condensates to intermediate degrees (k ~ 20−80; **Figs. 3b-c; S7**) as compared to other PLDs probed in this study.

a

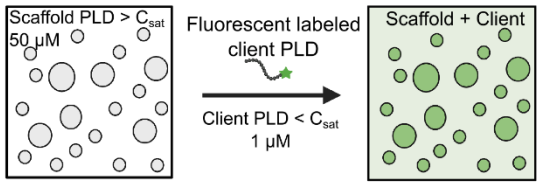

$$\text{Partition Coefficient } (k) = \frac{\text{Intensity in dense phase } (I_{dense})}{\text{Intensity in dilute phase } (I_{dilute})}$$

b

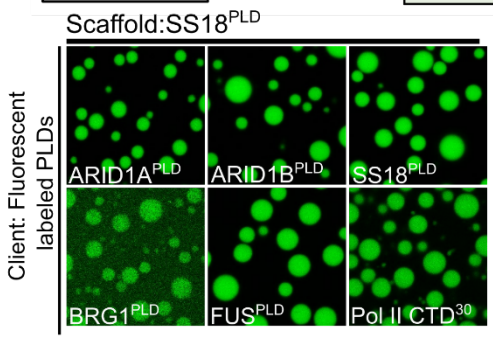

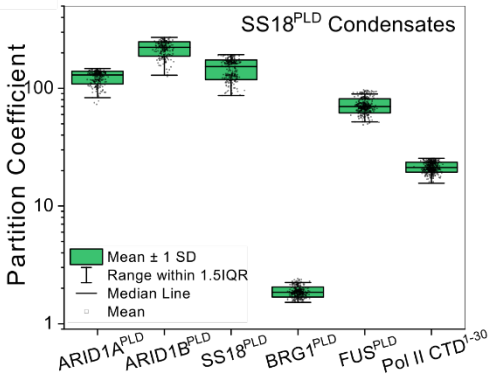

c

Partition coefficient of client (k)

Scaffold	ARID1A^{PLD} (523 aa)	ARID1B^{PLD} (403 aa)	SS18^{PLD} (352 aa)	BRG1^{PLD} (340 aa)	FUS^{PLD} (177 aa)	Pol II CTD^{30} (210 aa)
ARID1A^{PLD}	54.5 ± 4.1	104.5 ± 7.1	51.5 ± 6.6	3.5 ± .31	53.3 ± 38.9	40.2 ± 15.37
ARID1B^{PLD}	87.9 ± 5.5	177.3 ± 32.8	162.39 ± 20.2	5.5 ± .88	185.4 ± 36.6	78.9 ± 13.3
SS18^{PLD}	124.4 ± 15.6	218.3 ± 30.4	146.5 ± 27.7	1.8 ± .18	71.5 ± 9.9	21.4 ± 2.1

d

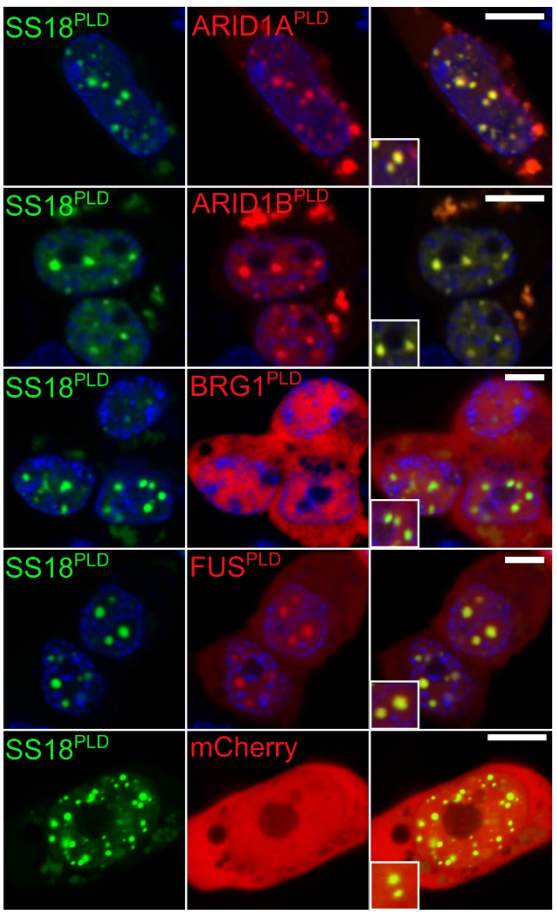

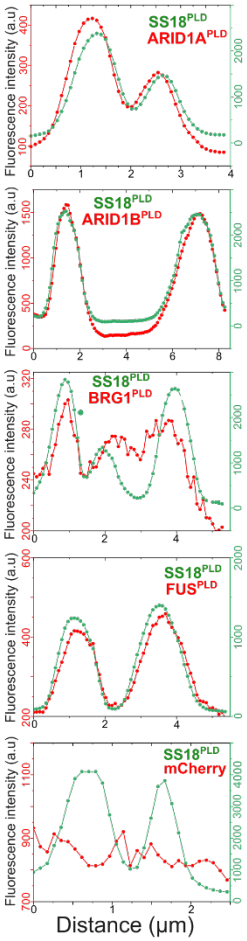

Figure 3: Heterotypic PLDs interact and enrich within homotypic PLD condensates. a) A Schematic of the co-partitioning assay based on confocal fluorescence microscopy. 50 μM concentration of the scaffold^{PLD} was used to form condensates and ~1 μM of the AlexaFluor488 labeled client^{PLD} was utilized to determine the partition coefficient (k). Created with BioRender.com. **b)** Partitioning of AlexaFluor488 labeled client PLDs (ARID1A^{PLD}, ARID1B^{PLD}, SS18^{PLD}, BRG1^{PLD}, RNA Polymerase II CTD[30], and FUS^{PLD}) within condensates of SS18^{PLD}. Enrichment (partition coefficient) is calculated as shown in (a) and displayed as a box-and-whisker plot. (n ≥ 100 condensates). **c)** The average partition coefficient (k) is tabulated along with the standard deviation from the mean. **d)** HEK293T cells co-expressing GFP-SS18^{PLD} and either one of the mCherry-tagged PLDs (ARID1A^{PLD}, ARID1B^{PLD}, FUS^{PLD} and BRG1^{PLD}) or mCherry alone. The degree of colocalization is displayed as intensity profiles for condensates shown in the *inset* images. Green represents the intensity profile of GFP-SS18^{PLD} and red represents the profile for mCherry-tagged PLDs. The enrichment coefficients are reported in **Fig. S9**. The scale bar is 10 μm.

Collective analysis of the experimental trend of partition coefficient data revealed a more positive correlation with the number of aromatic and arginine residues of the respective PLD chains (**Fig. S8**) than any other sequence features including the net charge per residues (NCPRs), number of hydrophobic residues, and PLD chain length. This observation indicates that the aromatic and arginine residues may drive homotypic phase separation of the system as well as heterotypic PLD-PLD interactions leading to their co-partitioning [66]. However, we note that although aromatic and arginine residues showed the highest correlation (R^2= 0.59) in our dataset, the overall low value of correlation suggests there exists a more complex interplay of interactions and chain solvation likely encoded by residues beyond these two residues.

Heterotypic interactions drive PLD co-condensation in live cells

Based on the observed extent of heterotypic PLD interactions among mSWI/SNF subunit PLDs and with FUS^{PLD} in our in vitro co-partitioning assay (**Fig. 3a-c**), we next asked whether mSWI/SNF PLDs interact with each other and form co-condensates in living cells. To test this, we co-expressed pairs of PLDs with a GFP tag and a mCherry tag, respectively. In our first set of studies, we took advantage of the very low C_{sat} of SS18^{PLD}, which forms condensates robustly upon low expression in the cell nucleus and is considered the scaffold PLD for live cell experiments. Heterotypic PLD interactions within phase-separated GFP-tagged SS18^{PLD} condensates in live cells were probed by the degree of mCherry-tagged PLD co-partitioning. mCherry alone was used as a reference in our experiments. We observed that when expressed together, PLD mixtures formed heterotypic co-condensates in cellulo, despite their abilities to form homotypic condensates (**Fig. 3d**). This observation further supports the idea that there exists a substantial overlap between homo- and hetero-complementarity of PLD interactions in these functionally-linked PLD systems. Quantification of the degree of enrichment revealed that while ARID1A and ARID1B are strongly colocalized with SS18^{PLD} in condensates (k > 2.0), BRG1^{PLD} only exhibited mildly enhanced enrichment (k = 1.09) compared to the mCherry control (k = 0.99, whereas FUS^{PLD} showed a strong level of colocalization (k = 1.53; **Fig. S9**). This observed trend in our cellular assays is consistent with our results from in vitro partitioning experiments performed with purified proteins (**Fig. 3b-c**), further supporting that heterotypic PLD interactions are likely to be sequence-specific. We next performed similar experiments with GFP-tagged ARID1A^{PLD} (**Fig. S10**) and ARID1B^{PLD} (**Fig. S11**) as scaffold condensates and made similar observations that except for BRG1^{PLD}, other PLDs strongly co-localize together in the dense phase. However, we noted that Pol II CTD[30] did not significantly enrich within condensates of any of the three mSWI/SNF PLDs in cells (**Fig. S12**). This observation contrasts with our in vitro client recruitment

assay results showing an enrichment coefficient k ~ 20−80 (**Fig. 3c**). This may be due to post-translational modification of the Pol II CTD in cells, specifically, phosphorylation, which was previously shown to inhibit Pol II CTD recruitment to condensates formed by the FET family PLDs [67].

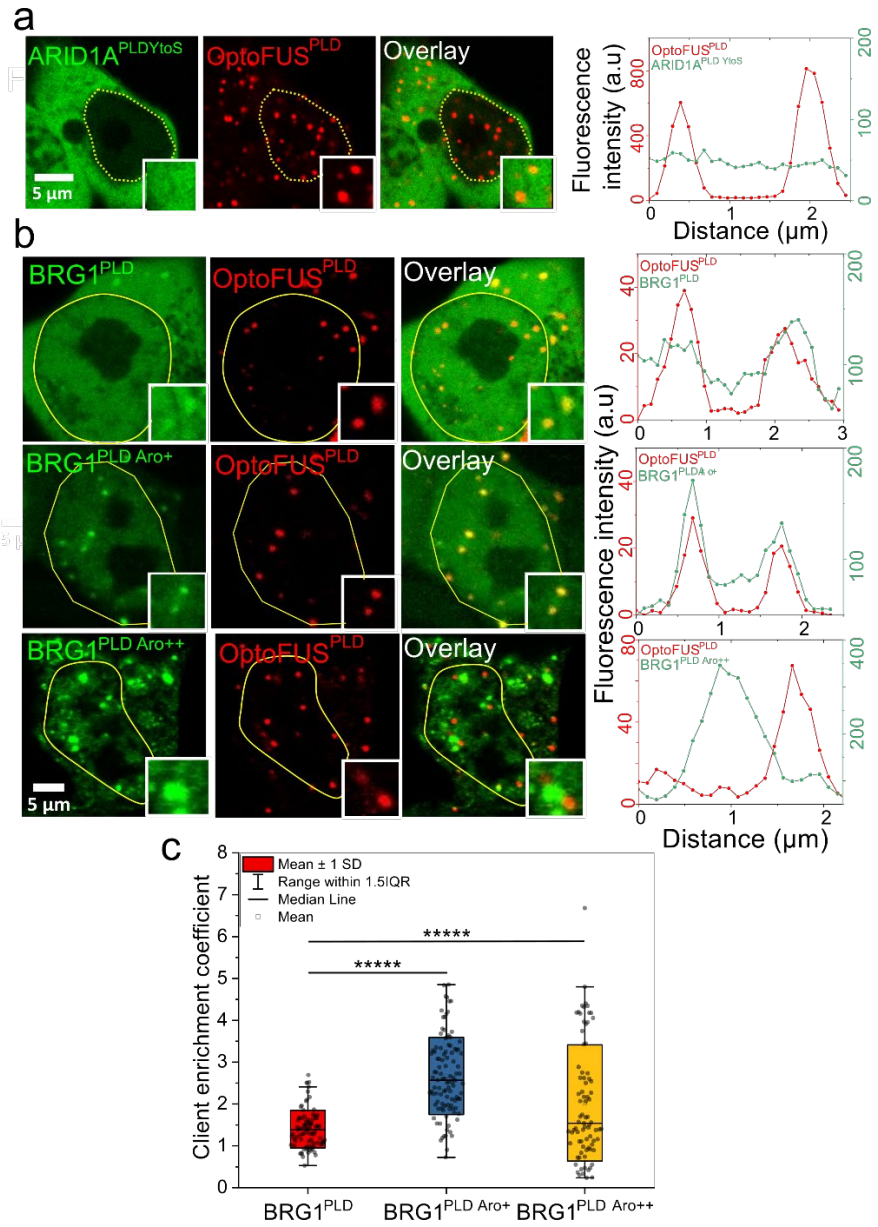

Figure 4: Tyrosine residues are important for heterotypic interactions within mSWI/SNF PLD condensates. a) HEK293T cells co-expressing GFP-tagged ARID1A$^{PLD\ YtoS}$ and mCherry-tagged OptoFUS^{PLD} construct. The degree of colocalization is displayed as intensity profiles for condensates shown in the inset images. Green represents the intensity profile of the GFP-tagged construct and red represents the profile for mCherry-tagged construct. **b)** HEK293T cells co-expressing PLDs (BRG1^{PLD}, BRG1$^{PLD\ Aro+}$, BRG1$^{PLD\ Aro++}$) and mCherry-tagged OptoFUS^{PLD} construct. The degree of colocalization is displayed as intensity profiles for condensates shown in the inset images. Green represents the intensity profile of the GFP-tagged construct and red represents the profile for mCherry-tagged construct. The yellow line indicates the nuclear periphery. **c)** Enrichment coefficients of GFP-tagged BRG1 PLDs within mCherry-tagged OptoFUS^{PLD} condensates. Enrichment is calculated as the ratio of mean intensities from the dense phase and

the dilute phase (n = 80-100 condensates from two replicates). Significance was calculated by a two-tailed t-test; ***** P ≤ 0.00001.

Tyrosine residues are important for both homotypic and heterotypic interactions within mSWI/SNF PLD condensates

Results described in Figure 2 above suggest that Tyr residues play an important role in driving homotypic phase separation of mSWI/SNF PLDs as well as the FUS^{PLD}. Due to the strong propensity of these distinct PLDs to colocalize in condensates, we next aimed to investigate the role of tyrosine residues in heterotypic PLD co-condensation. We first examined heterotypic interactions between FUS^{PLD} and a variant of $ARID1A^{PLD}$ lacking tyrosine residues (**Fig. 2c; Table S4**). As discussed above, the native $ARID1A^{PLD}$ condensates enrich FUS^{PLD} in live cells (**Fig. S10**). However, when $OptoFUS^{PLD}$ was co-expressed with the 29Y-to-S variant of ARID1A ($ARID1A^{PLD\ YtoS}$), we observed that $OptoFUS^{PLD}$ condensates did not enrich $ARID1A^{PLD\ YtoS}$, suggesting a loss of heterotypic interactions (**Fig. 4a**). To test if increasing the Tyr content of a PLD chain can increase the degree of co-ocalization, we performed a similar experiment with two $BRG1^{PLD}$ variants containing 17 ($BRG1^{PLD\ Aro+}$) and 41 ($BRG1^{PLD\ Aro++}$) additional Tyr residues, respectively. We observe the $BRG1^{PLD\ Aro+}$ variant has almost 2-fold greater enrichment within the $OptoFUS^{PLD}$ condensates compared to the $BRG1^{PLD}$. For $BRG1^{PLD\ Aro++}$ variant, however, we observed that the $OptoFUS^{PLD}$ condensates that formed on blue light activation did not show enrichment of $BRG1^{PLD\ Aro++}$, but pre-existing condensates of $BRG1^{PLD\ Aro++}$ were able to enrich $OptoFUS^{PLD}$ to a greater extent than WT $BRG1^{PLD}$ (**Fig. 4b-c**). Given $BRG1^{PLD\ Aro++}$ variant formed large irregular cytoplasmic aggregates in the cell, this may imply that in this case, the $BRG1^{PLD\ Aro++}$ homotypic interactions may have outweighed the heterotypic interactions, thereby driving the formation of discrete condensates similar to what was recently reported in the case of disordered FUS^{PLD} and $LAF1^{RGG}$ systems [43]. It is also possible that $BRG1^{PLD\ Aro++}$ condensates are viscoelastic solids, and their formation has resulted in a near-complete depletion of the soluble fraction of this PLD. Taken together with the data shown in Fig. 2, these results suggest that tyrosine residues are important for both homotypic and heterotypic interactions among mSWI/SNF PLD and FUS^{PLD} condensates.

PLD condensates exhibit specificity in interactions with functionally-linked IDRs

Our data in Figure 4 showing 29Y-to-S mutations of ARID1A abolishes the heterotypic interactions with FUS^{PLD} suggesting that there is a specificity of interactions among functionally-linked IDRs [68], which is likely to be encoded at the sequence level. To test the idea further, we attempted to probe interactions between PLD condensates with a naturally occurring non-prion-like IDR from a functionally unrelated protein. Since PLDs are predominantly associated with transcriptional activators and RNA-binding proteins [4], we reasoned to test if IDRs from a transcriptional repressor protein would enrich within PLD condensates. To this end, we choose the N-terminal IDR of FOXG1, which is a transcription factor predominantly acting as a transcriptional repressor in the developing brain [69]. The FOXG1 IDR contains 181 amino acids, comparable to FUS^{PLD} (**Fig. 5a**), and has low aromaticity (**Fig. 5b**), and does not form condensates when overexpressed in cells (**Fig. S13a**). To probe interactions of $FOXG1^{N\text{-}IDR}$ with PLDs, we created condensates of recombinantly purified FUS^{PLD} and $SS18^{PLD}$ and measured the enrichment coefficient of

AlexaFluor488 labeled FOXG1$^{N\text{-}IDR}$. We observed that both condensates *exclude* FOXG1$^{N\text{-}IDR}$ (enrichment coefficient < 1; **Fig. 5c-d**). In condensates of recombinant ARID1A^{PLD} and ARID1B^{PLD}, there was a slight enrichment of FOXG1$^{N\text{-}IDR}$, but the partitioning was at least 2-fold lower than BRG1^{PLD}, which was the weakest PLD probed in this study in terms strength of heterotypic interactions (**Figs. S13b-c**).

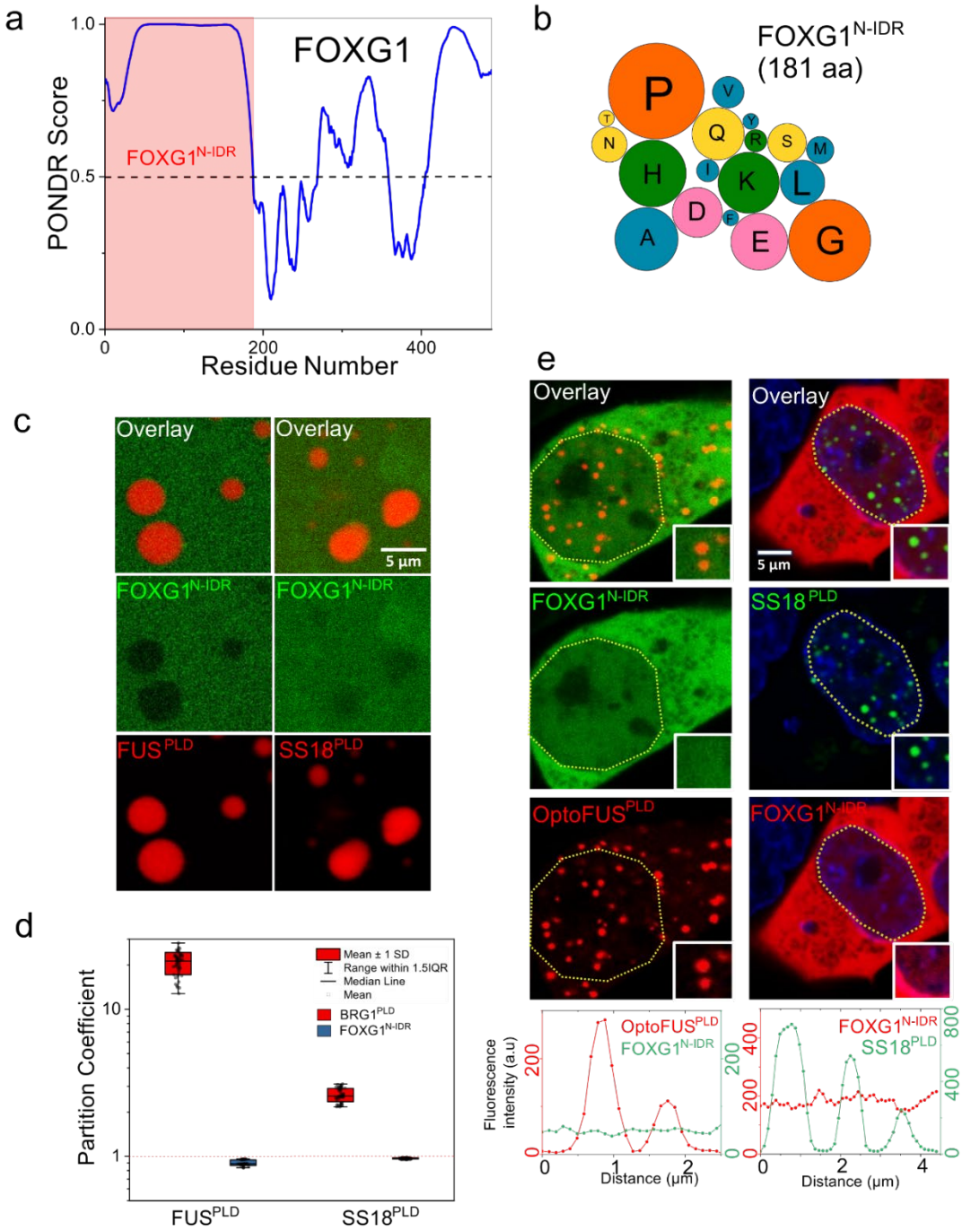

Figure 5: Selectivity in IDR interactions with condensates formed by prion-like domains. a) The PONDR score showing regions of disorder (>0.5) for the FOXG1 protein. The region shaded in red shows the N-terminus IDR for

FOXG1 used in the study. **b)** Amino acid composition of FOXG1$^{N\text{-}IDR}$. The color codes for amino acids are provided in Table S6. **c)** Partitioning of AlexaFluor488 labeled FOXG1$^{N\text{-}IDR}$ within condensates of FUS^{PLD} (250 μM) and SS18^{PLD} (50 μM), respectively. **d)** Enrichment is calculated as partition coefficient and displayed as a box-and-whisker plot for both FOXG1$^{N\text{-}IDR}$ and BRG1^{PLD} within these condensates (n = total of 25-50 droplets from two replicates). **e)** HEK293T cells co-expressing SS18^{PLD} and mCherry-tagged FOXG1$^{N\text{-}IDR}$ or GFP-tagged FOXG1$^{N\text{-}IDR}$ and OptoFUS^{PLD} constructs. The degree of colocalization is displayed as intensity profiles for condensates shown in the inset images. Green represents the intensity profile of GFP-tagged protein and red represents the profile for mCherry-tagged protein.

Based on the above results, we next tested if these observations hold in the context of live cells by co-expressing FOXG1$^{N\text{-}IDR}$ with either SS18^{PLD}, ARID1A^{PLD}, ARID1B^{PLD,} or OptoFUS^{PLD} condensates (**Figs. 5e; S13d**). In all cases, there was no enrichment of FOXG1$^{N\text{-}IDR}$ in any of the PLD condensates. Therefore, although the primary sequence of FOXG1$^{N\text{-}IDR}$ features similar spacer residues such as Pro, Gly, Gln, and Ser, partly similar to mSWI/SNF PLDs, it does not engage in heterotypic interactions with PLD condensates. Finally, to test if PLDs alone can be sufficient to explain the enrichment of a full-length mSWI/SNF subunit in FUS^{PLD} condensates, we tested the folded domain of BRG1 for its ability to interact with FUS^{PLD} condensates. We observed that the GFP-tagged BRG1^{Folded} does not enrich within OptoFUS^{PLD} condensates while both BRG1^{PLD} and full-length BRG1 do (**Fig. S14**). These results collectively suggest the existence of a sequence grammar that encodes interactions among PLDs from functionally related proteins and between PLDs and non-prion-like IDRs of distinct sequence complexity as well as full-length proteins.

mSWI/SNF PLDs lower the saturation concentration of FUS^{PLD} and form spatially homogeneous co-condensates

How do heterotypic PLD interactions impact the phase behavior of multi-component PLD mixtures encompassing FUS and mSWI/SNF subunit PLDs? To systematically address this, we chose FUS^{PLD} as our primary PLD system, which phase separates with a saturation concentration of ~ 200 μM in vitro (**Fig. S2a**), giving us a broad range of concentrations to test. To probe how mSWI/SNF PLDs affect FUS^{PLD} phase separation, we choose two specific PLD systems: ARID1A^{PLD}, which features strong heterotypic interactions with FUS^{PLD}, and BRG1^{PLD} that has weak heterotypic interactions with FUS^{PLD} (**Figs. S7; 5d**). While FUS^{PLD} ($C_{\text{sat}} \sim 200$ μM) has moderate phase separation driving force, BRG1^{PLD} (C_{sat} > 200 μM) has a substantially lower tendency to undergo phase separation and ARID1A^{PLD} (C_{sat} = 2.5 μM) is highly phase separation competent (**Figs. 1; S2a**). We observed that in the presence of both ARID1A^{PLD} and BRG1^{PLD} at concentrations below their respective C_{sat}, the saturation concentration of FUS^{PLD} is lowered in a non-linear fashion (**Figs. 6a**; **S15**). These observations suggest that heterotypic interactions are highly cooperative with homotypic interactions in driving phase separation of the PLD mixtures [69]. In the co-PLD phase diagram (**Fig. 6a**), we identify five specific regimes: regimes (I) and (V) are homotypic phase separation regimes of the two PLDs; regime (II) is a single-phase regime where the mixture of PLDs stay soluble; regime (III) is a PLD co-condensation regime where each of the component PLD concentrations is less than their respective C_{sat} but the mixture undergoes phase separation, and regime (IV) is another PLD co-condensation regime where each of the component PLD concentrations is higher than their respective C_{sat}.

Two emergent features of the two-component PLD phase diagrams (**Figs. 6a** & **S15**) are worth highlighting. The first of them is our observation that the PLD mixtures co-phase separate under conditions where the single PLD component concentrations are below their respective C_{sat} (regime III). In biomolecular mixtures of multiple PLD components, the phase separation driving

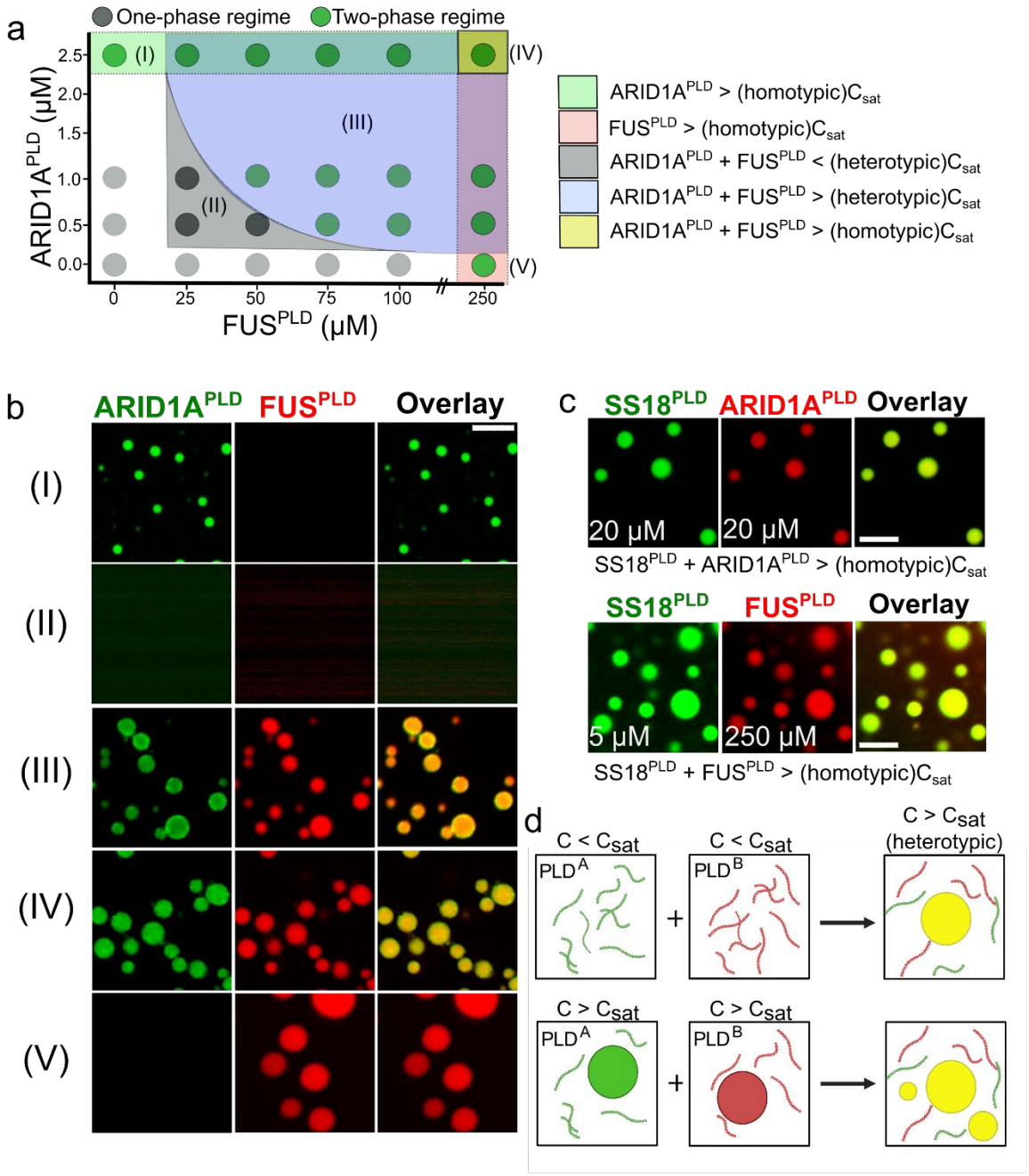

Figure 6: Heterotypic PLD interactions promote phase separation and form monophasic PLD co-condensates. a) Co-phase diagram of FUS^{PLD} and $ARID1A^{PLD}$ shows lowering of saturation concentration of heterotypic PLD mixtures. The green circles indicate two-phase regimes, and the grey circles indicate single-phase regimes. The legend describes the shaded regions highlighted in five distinct colors. **b)** Fluorescence microscopy images of PLD samples from the specific regions of the phase diagram shown in (**a**). $ARID1A^{PLD}$ is labeled with AlexaFluor488 and FUS^{PLD} is

labeled with AlexaFluor594. **c)** Fluorescence microscopy images of PLD co-condensates formed by the mixtures of SS18^{PLD} with ARID1A^{PLD} (top) and SS18^{PLD} with FUS^{PLD} (bottom) at concentrations above the saturation concentrations of respective PLDs. SS18^{PLD} is labeled with AlexaFluor488, ARID1A^{PLD}, and FUS^{PLD} are labeled with AlexaFluor594, respectively. The scale bar is 5 microns for all images. **d)** A schematic showing the formation of monophasic PLD co-condensates, corresponding to regimes III and IV in the phase diagram shown in (**a**). This is created with BioRender.com.

forces are effectively determined by the synergistic balance of homotypic and heterotypic PLD interactions. Intriguingly, the lowering of C_{sat} of FUS^{PLD} by mSWI/SNF subunit PLDs (**Figs. 6a** & **S15**) shows a concave trend, which is indicative of positive cooperativity where the heterotypic interactions enhance the phase separation of the mixture [70,71]. Therefore, in this case, the heterotypic PLD interactions dominate over the homotypic interactions leading to an effective lowering of the C_{sat} of either of the PLD chains.

The second key feature of the PLD mixture is the mixing of PLD dense phases within the co-condensates even though the C_{sat} of individual PLDs differ by almost two orders of magnitude (**Figs. 1**; **S2a**). This is evident from confocal fluorescence microscopy images, which revealed that the PLD mixtures formed co-condensates that are spatially homogeneous in regimes III and IV (**Figs. 6a-c**). The mixing of individual PLD phases and the formation of PLD co-condensates (**Fig. 6d**) was not only observed in vitro but also in live cells when two PLDs were co-expressed (**Figs. 3d** & **S10-11**). These observations again suggest that the sequence grammar driving homotypic and heterotypic PLD interactions are highly similar, leading to the dominance of heterotypic interactions in these mixtures (**Figs. 6a**; **S15**). If the homotypic chain interactions were dominant over heterotypic interactions in the PLD mixtures, multi-phasic condensate morphologies may emerge [43,53,70,71] with spatially co-existing individual PLD phases, which is the opposite of our experimental observations.

Heterotypic PLD interactions are detectable in the sub-saturation conditions

In our experiments thus far, we observed that condensates formed by mSWI/SNF subunit PLDs can recruit other PLDs in vitro and in live cells. Further, heterotypic PLD interactions lead to a lowering of FUS^{PLD} saturation concentration and the formation of spatially homogeneous PLD co-condensates. Since heterotypic interactions seem to dominate over homotypic interactions in PLD mixtures (**Fig. 6**; **Fig. S15**), we next asked whether these PLDs interact with each other at concentrations below their saturation concentrations and if their interactions in the dilute phase are also governed by the LCD primary sequence features. To address this, we first employed a bead halo assay [72] with a pair of PLDs. In these experiments, AlexaFluor488-labeled scaffold PLDs containing a hexahistidine (His_6) tag were immobilized on the surface of Ni-NTA micro-spheres through Ni-His_6 interactions. The scaffold PLD was designed to contain a solubility tag (MBP; *see* Materials and Methods) to abrogate homotypic phase separation on the bead surface. We used two mSWI/SNF PLDs, SS18^{PLD} and BRG1^{PLD}, as scaffolds in our experiments. The bulk scaffold PLD concentration used for these measurements was fixed at 250 nM, which is much lower than their respective C_{sat}. As a negative control, we used an AlexaFluor488-labeled His_6-MBP containing a short linker peptide (GGGCGGG) without any PLDs. Next, 250 nM of AlexaFluor594-labeled FUS^{PLD} (client PLD) was added to the solution (**Fig. 7a**). We expect that if heterotypic PLD

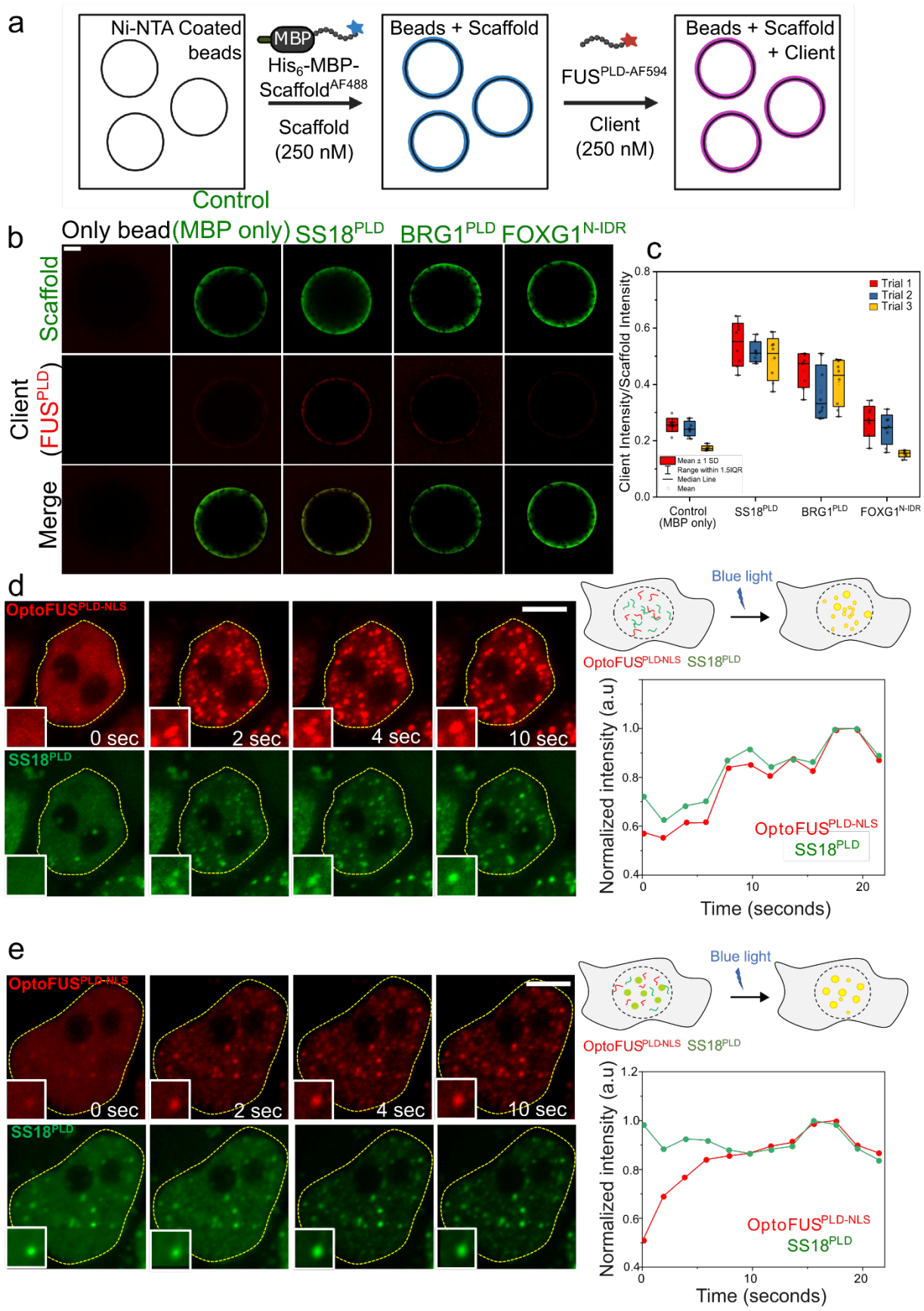
a
Ni-NTA Coated beads
MBP
His6-MBP-Scaffold AF488
Scaffold (250 nM)
Beads + Scaffold
FUS PLD-AF594
Client (250 nM)
Beads + Scaffold + Client
Control
b
Only bead (MBP only)
SS18 PLD
BRG1 PLD
FOXG1 N-IDR
Scaffold
Client (FUS PLD)
Merge
c
Client Intensity/Scaffold Intensity
Trial 1
Trial 2
Trial 3
Mean ± 1 SD
Range within 1.5IQR
Median Line
Mean
Control (MBP only)
SS18 PLD
BRG1 PLD
FOXG1 N-IDR
d
OptoFUS PLD-NLS
SS18 PLD
0 sec
2 sec
4 sec
10 sec
Blue light
Normalized intensity (a.u)
Time (seconds)
e
OptoFUS PLD-NLS
SS18 PLD
0 sec
2 sec
4 sec
10 sec
Blue light
Normalized intensity (a.u)
Time (seconds)

Figure 7: Heterotypic PLDs interact at sub-saturation concentrations. a) A schematic representation of the bead halo assay. Created with BioRender.com. **b)** 250 nM of AlexaFluor488-labeled His_6-MBP-constructs – $SS18^{PLD}$, $BRG1^{PLD}$, $FOXG1^{N\text{-}IDR}$, or control His_6-MBP-GGGCGGG was attached to Ni-NTA beads. 250 nM of FUS^{PLD} labeled with AlexaFluor594 was then added to the above beads (*see* Materials and Methods for further details). Binding was quantified using the ratio of fluorescence intensities (fluorescence signal from FUS^{PLD}/fluorescence signal from the scaffold) on the surface of the bead. **c)** A box-and-whisker chart of the intensity ratios is plotted with the mean and standard deviation (n = 8 beads/ trial). Significance is shown in **Fig. S16**. **d)** HEK293T cells co-expressing $OptoFUS^{PLD\text{-}NLS}$ (Cry2-mCherry-$FUS^{PLD\text{-}NLS}$) and GFP-$SS18^{PLD}$ below their saturation concentrations. Upon blue light activation, $OptoFUS^{PLD}$ co-condenses with GFP-$SS18^{PLD}$. Mean intensity profiles of the co-condensates formed are shown as a function of time for condensates within the inset image. Green represents the intensity profile of GFP-$SS18^{PLD}$ and red represents the intensity profile for $OptoFUS^{PLD}$. The corresponding movie is shown in **Movie S1**. **e)** Pre-existing GFP-$SS18^{PLD}$ clusters act as nucleation sites for $OptoFUS^{PLD}$ condensates upon blue light activation (also see **Movie S2** & **Movie S3)**. The scale bar is 5 μm for all images.

interactions are present at these scaffold-client concentrations that are much lower than their C_{sat}, they would enable the recruitment of the client PLD (FUS^{PLD}) to the bead surfaces coated with a scaffold PLD ($SS18^{PLD}$ or $BRG1^{PLD}$). Further, the relative degree of client recruitment will depend on the relative strength of scaffold-client interactions (**Fig. 3**). Indeed, we observed that FUS^{PLD} is preferentially recruited on the $SS18^{PLD}$- and $BRG1^{PLD}$-coated beads whereas beads coated with MBP-alone did not show such client enrichment (**Fig. 7b-c**). These data suggest that $SS18^{PLD}$ and $BRG1^{PLD}$ interact with FUS^{PLD} at a concentration much lower than their saturation concentrations. We further noted that the relative FUS^{PLD} enrichment was much higher on $SS18^{PLD}$-coated beads as compared to $BRG1^{PLD}$-coated beads (**Fig. 7c; S16**), suggesting that $SS18^{PLD}$ is a significantly stronger scaffold than the $BRG1^{PLD}$. We also compared these results with a non-prion-like IDR, $FOXG1^{N\text{-}IDR}$, which was found to be non-interactive with PLD condensates in vitro and in live cells (**Fig. 5**). Similar to the MBP control, $FOXG1^{N\text{-}IDR}$-coated beads failed to recruit FUS^{PLD}. These results not only provide evidence of the presence of heterotypic PLD-PLD interactions at their sub-saturation concentrations but also lend further support that the heterotypic interactions between FUS^{PLD} and mSWI/SNF component PLDs are sequence-specific (**Fig. 7c**). We also attempted to quantify apparent binding affinities by titrating FUS^{PLD} concentration and keeping the scaffold PLD concentration fixed. However, instead of an apparent two-state binding isotherm, we observed a monotonic increase in the enrichment of FUS^{PLD} on the bead surface (**Fig. S17**) as the FUS^{PLD} concentration increased. This observation may suggest non-stoichiometric binding and homotypic interactions between the FUS^{PLD} chains on the surface of the bead at higher client concentrations [73,74].

The occurrence of heterogeneous nanoscopic oligomers of FUS in the pre-phase separation regime has recently been reported [50]. Our observations that heterotypic PLDs interact and recruit each other on the bead surface at concentrations much lower than their saturation concentrations now suggest that heterotypic interactions between prion-like LCDs can also occur in the dilute phase independent of phase separation. However, a key unanswered question is whether such interactions can be observed in the complex intracellular microenvironment of a living cell. To test heterotypic interactions between mSWI/SNF subunit PLDs and FUS^{PLD} in the absence of phase separation, we employed a light-activated phase separation approach [48,49,73,74]. In this assay, we used an $OptoFUS^{PLD\text{-}NLS}$ construct to induce FUS^{PLD} condensation in live cell nucleus using blue light, while co-expressing GFP-$SS18^{PLD}$ near sub-saturation level (**Fig. 7d**). When FUS^{PLD} condensation was actuated by blue light, we made two key observations. The first one was that $SS18^{PLD}$ was enriched simultaneously at sites where $OptoFUS^{PLD\text{-}NLS}$ condensates

were formed upon blue light activation (**Fig. 7d; Movie S1**). We note that in this case, there were no pre-existing SS18^{PLD} condensates. Secondly, we observed that in cells containing pre-existing SS18^{PLD} clusters, they acted as nucleation centers for OptoFUS^{PLD} condensation (**Fig. 7e; Movie S2**). This feature is further highlighted in cells with multiple pre-existing SS18^{PLD} condensates where OptoFUS^{PLD} condensation only occurred at those sites (**Fig. S18; Movie S3**). Collectively, we conclude that FUS and SS18 PLDs form soluble complexes in the dilute phase below their saturation concentrations and SS18^{PLD} clusters can nucleate condensation of the FUS^{PLD} in live cells (**Figs. 7d-e; S18**).

Discussion

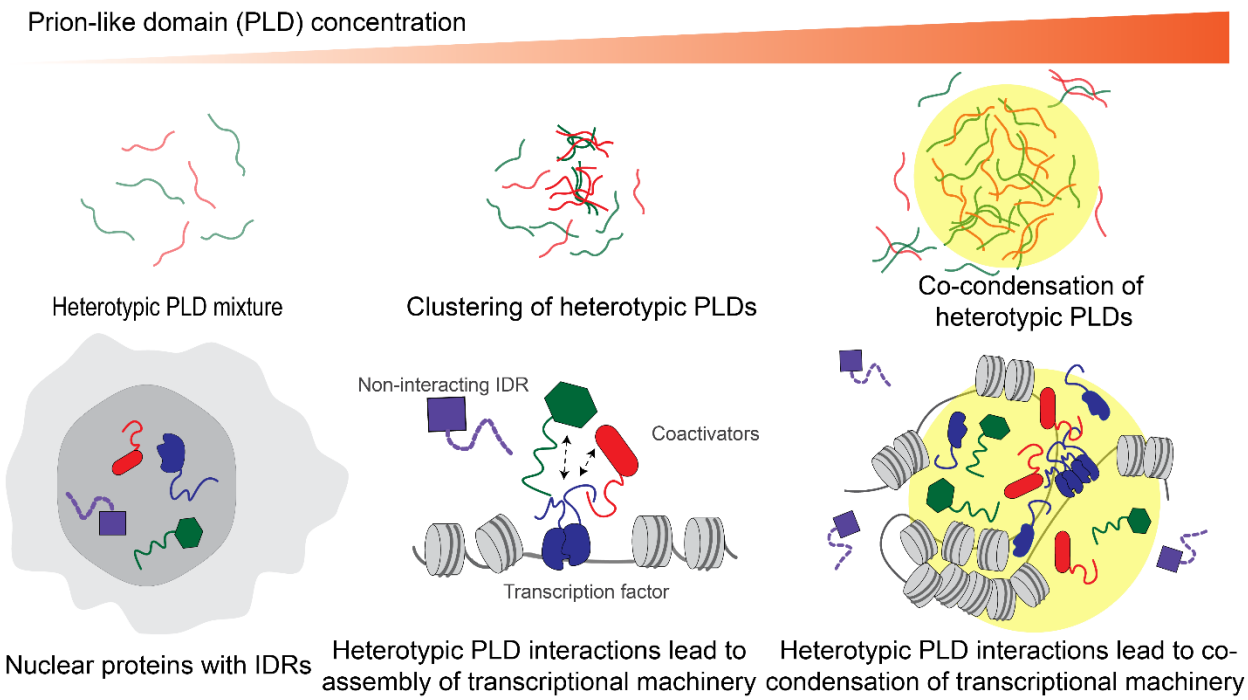

Figure 8: Schematic illustration of heterotypic PLD-mediated co-assemblies driving functional protein interaction networks. Heterotypic PLD interactions occur in the dilute phase at sub-saturation concentrations which upon increasing protein concentration can lead to co-phase separation of the mixture into spatially homogeneous multi-component condensates (top panel). Our results collectively suggest that transcriptional proteins can be assembled into co-phase-separated hubs through sequence-specific positively cooperative interactions among low-complexity domains (bottom panel).

mSWI/SNF (also known as BAF) complex is a multi-subunit ATP-dependent chromatin remodeler with critical functions in genome organization and spatiotemporal transcriptional programming during development [48,49,75,76]. Mutations in mSWI/SNF subunits including ARID1A/B, BRG1, and SS18 are linked to multiple tumor types. However, apart from the ATP-dependent catalytic activity of the subunit BRG1 in nucleosome repositioning and eviction [77,78], the functions of other subunits in controlling chromatin landscape are less understood. Interestingly, one common feature among ARID1A/B, BRG1, and SS18 primary sequences is that they all have long stretches (~ 300-500 amino acids) of disordered low-complexity domains without any known

functions [32,40,41,81,82]. Sequence analysis revealed that these LCDs are prion-like (**Fig. S1**) [41,46]. Employing in vitro experiments with purified LCDs as well as cell culture models, here we show that AIRD1A/B and SS18 PLDs undergo liquid-liquid phase separation with saturation concentrations substantially lower than previously reported PLDs from RNA-binding proteins, including FUS^{PLD} (**Fig. 1**; **Fig. S2**). We hypothesized that similar to the PLDs from FET families [31,77–81], the tyrosine residues provide a major driving force for their high phase-separation capacity. We tested this idea by creating 29Tyr-to-Ser variant of $ARID1A^{PLD}$ and 17Pro-to-Tyr and 41Pro-to-Tyr variants of $BRG1^{PLD}$ (**Fig. 2c**). Mutations of Tyr residues abolished phase separation propensity of $ARID1A^{PLD}$ completely in cells, similar to mutating half the tyrosine residues of FUS^{2XPLD} to serine that resulted in a complete loss of phase separation (**Fig. 2b**), whereas introducing Tyr residues to $BRG1^{PLD}$ increased its propensity to form intracellular condensates significantly (**Fig. 2d**). We also made a 30Gln-to-Gly variants of $ARID1A^{PLD}$, which only increased the C_{sat} of $ARID1A^{PLD}$ ~ 2-fold. Together, these results suggest that Tyr residues are a key determinant of mSWI/SNF PLD phase separation, whereas polar residues such as Gln plays a modest role.

Not only in homotypic interactions, we found that Tyr residues play dominant roles in heterotypic PLD interactions between the mSWI/SNF PLDs and FUS^{PLD}. The key roles of aromatic amino acids in mSWI/SNF PLD phase separation and engagement with FUS^{PLD} may stem from the ability of Tyr residues to interact with multiple other residues including arginine, proline, and methionine in addition to aromatic residues [31,79–83]. Since mSWI/SNF subunit PLDs are enriched with proline and methionine residues (**Table S1-3**), the presence of aromatic amino acids can therefore magnify the number of multivalent contacts between PLD chains (**Fig. 1b**). This is further supported by the fact that inclusion of 17 Tyr residues to $BRG1^{PLD}$ was sufficient to improve its intracellular saturation concentration to a level comparable to other mSWI/SNF PLDs (**Fig. 2d**). While FUS^{PLD} and $FUS^{2XPLD\ halfYtoS}$ with 24 aromatic residues did not phase separate in cells, $BRG1^{PLD\ Aro+}$, which contains 24 aromatic residues, was able to form intracellular condensates at much lower expression level (**Fig. 2**). Our results, therefore, are consistent with a model for PLD phase separation where Tyr residues play a key role by mediating a diverse set of inter-chain interactions. Similarly, Tyr-mediated interactions are likely to play an equally important role in driving heterotypic PLD associations (**Figs. 4b-c; S8**), driving specificity in partner recruitment (**Fig. 5**), and formation of PLD co-condensates (**Fig. 6**). However, we also acknowledge that interactions mediated by non-aromatic residues can play a sizable role in shaping the overall phase behavior of the system, and uncovering them in the future studies will lead to a more complete picture of the underlying molecular grammar.

The saturation concentrations of the PLDs of SS18, ARID1A/B, and FUS^{PLD} differ by two orders of magnitude at room temperature (**Figs. 1; Fig. S2**), yet mSWI/SNF PLD condensates formed completely miscible co-condensates with FUS^{PLD} in vitro and in live cells (**Figs. 3** & **6**). This observation seems puzzling at first based on the difference in C_{sat} values of respective PLD chains, which may represent highly dissimilar strengths of homotypic inter-chain interactions in FUS^{PLD} and mSWI/SNF PLDs. If the homotypic interactions are substantially different in a mixture of IDRs, they can form coexisting dense phases with differential densities [43,53,70,71]. This is likely the case for $BRG1^{PLD\ Aro++}$ variant, which formed discrete condensed phases when co-expressed

with OptoFUS^{PLD} condensates (**Fig. 4b-c**). However, except for this synthetic variant, our co-phase diagrams in vitro (**Figs. 6**; **S15**) and PLD co-condensation results in live cells suggest that heterotypic interactions between mSWI/SNF PLD chains are dominant over the homotypic interactions in PLD mixtures. This assertion is consistent with the observed miscibility of FUS^{PLD} condensates with ARID1A^{PLD} and SS18^{PLD} condensates. The observed positive cooperativity in interactions between PLDs of mSWI/SNF subunits and that of FET proteins may have important functional relevance in the formation of transcriptional hubs where transcription factors and coactivators can coexist in a single homogeneous phase-separated hub through co-scaffolding (**Fig. 8**). This implies that multiple proteins with PLDs can provide a positive cooperative effect to reduce the concentration required for phase separation of the collection of proteins. We speculate that heterotypic PLD-mediated positive cooperativity in protein-protein interactions is likely to play key roles in the operation of SWI/SNF complexes and their interactions with transcription factors containing similar low-complexity domains [86]. Interestingly, FOXG1$^{N\text{-}IDR}$, a disordered non-prion-like domain of a transcriptional repressor, was observed to be excluded from PLD condensates in cells or has a very low enrichment coefficient in vitro (**Figs. 5; S13**), suggesting a complex sequence grammar that incorporates specificity within PLDs for partner interactions necessary for their biological functions.

The ability of the FET family of transcription factors containing an N-terminal PLD to orchestrate oncogenic gene expression has recently been linked to their aberrant interactions with the BAF complex subunits, such as BRG1[84–86]. Previously, heterotypic interactions have been reported for transcription factors containing PLDs such as EBF1 and FUS [86–88], as well as FET proteins and FUS-DDIT3 [87]. Given multiple mSWI/SNF subunits contain long PLDs, could such interactions be mediated by these intrinsically disordered LCDs (**Fig. 8**)? Indeed, our results suggest that mSWI/SNF subunit PLDs can engage in sequence-specific interactions with each other and with the PLD of FUS. We observe that FUS-DDIT3 condensates can enrich mSWI/SNF PLDs (**Fig. S19**) with an enrichment coefficient similar to what was observed for mSWI/SNF PLD-only condensates (**Figs. 3d; S9**). Since PLDs are common in many endogenous and cancer-associated fusion transcription factors, based on our results reported here, we speculate a common mode of functional protein-protein interactions in transcriptional regulation for these factors through sequence-specific heterotypic interactions between low-complexity protein domains.

Finally, a key finding of our study is that the PLD-mediated multivalent interactions can occur at sub-micromolar concentrations below their saturation concentrations (**Fig. 7**). These results imply that heterotypic PLD-mediated protein-protein interactions are likely to be present at physiologically relevant protein concentrations inside living cells. Such interactions can lead to the formation of heterotypic clusters at the single-phase regime, similar to homotypic pre-percolation clusters observed for RNA-binding proteins [89]. Given intracellular concentrations of many proteins at their endogenous level often resides at sub-saturation level [88], our results reported in this work suggest that the functional protein-protein networks can arise from heterotypic interactions mediated by multivalent LCDs in the dilute phase independent of phase separation.

Acknowledgments

This work was supported by the US National Institute of General Medical Sciences (NIGMS) of the National Institutes of Health grant award (R35 GM138186) to P.R.B. The initial part of this work was supported by the US National Institute on Aging (NIA) of the National Institutes of Health grant award (R21 AG064258) to P.R.B. The authors gratefully acknowledge the members of the Banerjee Lab, Dr. Rohit Pappu and Dr. Tanja Mittag for valuable feedback during the manuscript preparation.

Author contributions

Conceptualization: P.R.B. and R.B.D.; Methodology: P.R.B., R.B.D., A.S., and A.K.R.; Investigation: P.R.B., R.B.D., M.M.M., and A.K.R.; Resources: P.R.B.; Writing – original draft: P.R.B., M.M.M., and R.B.D.; Writing – reviewing and editing: P.R.B. and R.B.D.; Funding acquisition: P.R.B.

Competing interests

All authors declare no competing interests.

Data Availability

All data relevant to the findings of this manuscript are included in the manuscript and the supplementary appendix.

References

1. Banani, S. F., Lee, H. O., Hyman, A. A. & Rosen, M. K. Biomolecular condensates: organizers of cellular biochemistry. *Nat. Rev. Mol. Cell Biol.* **18**, 285–298 (2017).
2. Sabari, B. R., Dall'Agnese, A. & Young, R. A. Biomolecular Condensates in the Nucleus. *Trends Biochem. Sci.* **45**, 961–977 (2020).
3. Alberti, S. & Hyman, A. A. Biomolecular condensates at the nexus of cellular stress, protein aggregation disease and ageing. *Nat. Rev. Mol. Cell Biol.* **22**, 196–213 (2021).
4. March, Z. M., King, O. D. & Shorter, J. Prion-like domains as epigenetic regulators, scaffolds for subcellular organization, and drivers of neurodegenerative disease. *Brain Res.* **1647**, 9–18 (2016).
5. Farag, M., Borcherds, W. M., Bremer, A., Mittag, T. & Pappu, R. V. Phase separation of protein mixtures is driven by the interplay of homotypic and heterotypic interactions. *Nat. Commun.* **14**, 5527 (2023).
6. Lancaster, A. K., Nutter-Upham, A., Lindquist, S. & King, O. D. PLAAC: a web and command-line application to identify proteins with prion-like amino acid composition. *Bioinformatics* **30**, 2501–2502 (2014).
7. Alberti, S., Halfmann, R., King, O., Kapila, A. & Lindquist, S. A systematic survey identifies prions and illuminates sequence features of prionogenic proteins. *Cell* **137**, 146–158 (2009).
8. Tetz, G. & Tetz, V. Prion-like Domains in Eukaryotic Viruses. *Sci. Rep.* **8**, 8931 (2018).
9. Espinosa Angarica, V., Ventura, S. & Sancho, J. Discovering putative prion sequences in complete proteomes using probabilistic representations of Q/N-rich domains. *BMC Genomics* **14**, 316 (2013).
10. Zajkowski, T. *et al.* The Hunt for Ancient Prions: Archaeal Prion-Like Domains Form Amyloid-Based Epigenetic Elements. *Molecular Biology and Evolution* **38**, 2088–2103 (2021).
11. Garai, S. *et al.* Plant Prionome maps reveal specific roles of prion-like proteins in stress and memory. *bioRxiv* 2020.09.25.311993 (2020).
12. Tetz, G. & Tetz, V. Prion-Like Domains in Phagobiota. *Frontiers in Microbiology* **8**, 2239 (2017).
13. Murakami, T. *et al.* ALS/FTD Mutation-Induced Phase Transition of FUS Liquid Droplets and Reversible Hydrogels into Irreversible Hydrogels Impairs RNP Granule Function. *Neuron* **88**, 678–690 (2015).
14. King, O. D., Gitler, A. D. & Shorter, J. The tip of the iceberg: RNA-binding proteins with prion-like domains in neurodegenerative disease. *Brain Res.* **1462**, 61–80 (2012).
15. Jaunmuktane, Z. & Brandner, S. Invited Review: The role of prion-like mechanisms in neurodegenerative diseases. *Neuropathol. Appl. Neurobiol.* **46**, 522–545 (2020).
16. Fowler, D. M., Koulov, A. V., Balch, W. E. & Kelly, J. W. Functional amyloid--from bacteria to humans. *Trends Biochem. Sci.* **32**, 217–224 (2007).
17. Franzmann, T. M. & Alberti, S. Prion-like low-complexity sequences: Key regulators of protein solubility and phase behavior. *J. Biol. Chem.* **294**, 7128–7136 (2019).
18. Martin, E. W. *et al.* Valence and patterning of aromatic residues determine the phase behavior of prion-like domains. *Science* **367**, 694–699 (2020).
19. Bremer, A. *et al.* Deciphering how naturally occurring sequence features impact the phase behaviours of disordered prion-like domains. *Nat. Chem.* **14**, 196–207 (2022).
20. Molliex, A. *et al.* Phase separation by low complexity domains promotes stress granule assembly and drives pathological fibrillization. *Cell* **163**, 123–133 (2015).
21. Gotor, N. L. *et al.* RNA-binding and prion domains: the Yin and Yang of phase separation. *Nucleic Acids Res.* **48**, 9491–9504 (2020).

22. Boncella, A. E. *et al.* Composition-based prediction and rational manipulation of prion-like domain recruitment to stress granules. *Proc. Natl. Acad. Sci. U. S. A.* **117**, 5826–5835 (2020).
23. Choi, K.-J. *et al.* NANOG prion-like assembly mediates DNA bridging to facilitate chromatin reorganization and activation of pluripotency. *Nat. Cell Biol.* (2022) doi:10.1038/s41556-022-00896-x.
24. Davis, R. B., Moosa, M. M. & Banerjee, P. R. Ectopic biomolecular phase transitions: fusion proteins in cancer pathologies. *Trends Cell Biol.* **32**, 681–695 (2022).
25. Schwartz, J. C., Cech, T. R. & Parker, R. R. Biochemical Properties and Biological Functions of FET Proteins. *Annu. Rev. Biochem.* **84**, 355–379 (2015).
26. Lin, Y., Currie, S. L. & Rosen, M. K. Intrinsically disordered sequences enable modulation of protein phase separation through distributed tyrosine motifs. *J. Biol. Chem.* **292**, 19110–19120 (2017).
27. Johnson, C. N. *et al.* Insights into Molecular Diversity within the FET Family: Unraveling Phase Separation of the N-Terminal Low Complexity Domain from RNA-Binding Protein EWS. *bioRxiv* 2023.10.27.564484 (2023) doi:10.1101/2023.10.27.564484.
28. Julia Maristany, M., Gonzalez, A. A., Collepardo-Guevara, R. & Joseph, J. A. Universal predictive scaling laws of phase separation of prion-like low complexity domains. *bioRxiv* 2023.06.14.543914 (2023) doi:10.1101/2023.06.14.543914.
29. Rekhi, S. *et al.* Expanding the molecular language of protein liquid-liquid phase separation. *bioRxiv* 2023.03.02.530853 (2023) doi:10.1101/2023.03.02.530853.
30. Schuster, B. S. *et al.* Identifying sequence perturbations to an intrinsically disordered protein that determine its phase-separation behavior. *Proc. Natl. Acad. Sci. U. S. A.* **117**, 11421–11431 (2020).
31. Wang, J. *et al.* A Molecular Grammar Governing the Driving Forces for Phase Separation of Prion-like RNA Binding Proteins. *Cell* **174**, 688-699.e16 (2018).
32. Davis, R. B., Kaur, T., Moosa, M. M. & Banerjee, P. R. FUS oncofusion protein condensates recruit mSWI/SNF chromatin remodeler via heterotypic interactions between prion-like domains. *Protein Sci.* **30**, 1454–1466 (2021).
33. Owen, I. *et al.* The oncogenic transcription factor FUS-CHOP can undergo nuclear liquid-liquid phase separation. *bioRxiv* 2021.02.24.432743 (2021) doi:10.1101/2021.02.24.432743.
34. Patel, A. *et al.* A Liquid-to-Solid Phase Transition of the ALS Protein FUS Accelerated by Disease Mutation. *Cell* **162**, 1066–1077 (2015).
35. Zhang, Y.-J. *et al.* The dual functions of the extreme N-terminus of TDP-43 in regulating its biological activity and inclusion formation. *Hum. Mol. Genet.* **22**, 3112–3122 (2013).
36. Farag, M., Borcherds, W. M., Bremer, A., Mittag, T. & Pappu, R. V. Phase Separation in Mixtures of Prion-Like Low Complexity Domains is Driven by the Interplay of Homotypic and Heterotypic Interactions. *bioRxiv* 2023.03.15.532828 (2023) doi:10.1101/2023.03.15.532828.
37. Fomicheva, A. & Ross, E. D. From Prions to Stress Granules: Defining the Compositional Features of Prion-Like Domains That Promote Different Types of Assemblies. *Int. J. Mol. Sci.* **22**, (2021).
38. Harrison, A. F. & Shorter, J. RNA-binding proteins with prion-like domains in health and disease. *Biochem. J.* **474**, 1417–1438 (2017).
39. Frazer, C. *et al.* Epigenetic cell fate in Candida albicans is controlled by transcription factor condensates acting at super-enhancer-like elements. *Nature Microbiology* **5**, 1374–1389 (2020).
40. Wang, Y. *et al.* A Prion-like Domain in Transcription Factor EBF1 Promotes Phase Separation and Enables B Cell Programming of Progenitor Chromatin. *Immunity* **53**, 1151-1167.e6 (2020).

41. Boulay, G. *et al.* Cancer-Specific Retargeting of BAF Complexes by a Prion-like Domain. *Cell* **171**, 163-178.e19 (2017).
42. Huang, X. *et al.* Heterotypic transcriptional condensates formed by prion-like paralogous proteins canalize flowering transition in tomato. *Genome Biol.* **23**, 78 (2022).
43. Welles, R. M. *et al.* Determinants of disordered protein co-assembly into discrete condensed phases. *bioRxivorg* (2023) doi:10.1101/2023.03.10.532134.
44. Kar, M. *et al.* Phase-separating RNA-binding proteins form heterogeneous distributions of clusters in subsaturated solutions. *Proc. Natl. Acad. Sci. U. S. A.* **119**, e2202222119 (2022).
45. Deniz, A. A. Percolation physics and density transition frameworks converge in biomolecular condensation. *Proc. Natl. Acad. Sci. U. S. A.* **119**, e2210177119 (2022).
46. Lindén, M. *et al.* FET family fusion oncoproteins target the SWI/SNF chromatin remodeling complex. *EMBO Rep.* **20**, e45766 (2019).
47. Mittal, P. & Roberts, C. W. M. The SWI/SNF complex in cancer - biology, biomarkers and therapy. *Nat. Rev. Clin. Oncol.* **17**, 435–448 (2020).
48. Centore, R. C., Sandoval, G. J., Soares, L. M. M., Kadoch, C. & Chan, H. M. Mammalian SWI/SNF Chromatin Remodeling Complexes: Emerging Mechanisms and Therapeutic Strategies. *Trends Genet.* **36**, 936–950 (2020).
49. Kadoch, C. & Crabtree, G. R. Mammalian SWI/SNF chromatin remodeling complexes and cancer: Mechanistic insights gained from human genomics. *Sci. Adv.* **1**, e1500447 (2015).
50. El Hadidy, N. & Uversky, V. N. Intrinsic Disorder of the BAF Complex: Roles in Chromatin Remodeling and Disease Development. *Int. J. Mol. Sci.* **20**, (2019).
51. Thway, K. & Fisher, C. Synovial sarcoma: defining features and diagnostic evolution. *Ann. Diagn. Pathol.* **18**, 369–380 (2014).
52. Mittag, T. & Pappu, R. V. A conceptual framework for understanding phase separation and addressing open questions and challenges. *Mol. Cell* **82**, 2201–2214 (2022).
53. Kaur, T. *et al.* Sequence-encoded and composition-dependent protein-RNA interactions control multiphasic condensate morphologies. *Nat. Commun.* **12**, 872 (2021).
54. Varga, J., Kube, M., Luck, K. & Schick, S. The BAF chromatin remodeling complexes: structure, function, and synthetic lethalities. *Biochem. Soc. Trans.* **49**, 1489–1503 (2021).
55. Shin, Y. *et al.* Spatiotemporal Control of Intracellular Phase Transitions Using Light-Activated optoDroplets. *Cell* vol. 168 159-171.e14 (2017).
56. Burke, K. A., Janke, A. M., Rhine, C. L. & Fawzi, N. L. Residue-by-residue view of in vitro FUS granules that bind the C-terminal domain of RNA polymerase II. *Mol. Cell* **60**, 231–241 (2015).
57. Maharana, S. *et al.* RNA buffers the phase separation behavior of prion-like RNA binding proteins. *Science* **360**, 918–921 (2018).
58. Hofweber, M. & Dormann, D. Friend or foe-Post-translational modifications as regulators of phase separation and RNP granule dynamics. *J. Biol. Chem.* **294**, 7137–7150 (2019).
59. Guilak, F., Tedrow, J. R. & Burgkart, R. Viscoelastic properties of the cell nucleus. *Biochem. Biophys. Res. Commun.* **269**, 781–786 (2000).
60. Rosowski, K. A. *et al.* Elastic ripening and inhibition of liquid-liquid phase separation. *Nat. Phys.* **16**, 422–425 (2020).
61. Zhang, Y., Lee, D. S., Meir, Y., Brangwynne, C. P. & Wingreen, N. S. Mechanical frustration of phase separation in the cell nucleus by chromatin. *Biophys. J.* **122**, 6a (2023).
62. Roggero, C. M. *et al.* Poly-glutamine-dependent self-association as a potential mechanism for regulation of androgen receptor activity. *PLoS One* **17**, e0258876 (2022).
63. Hutin, S. *et al.* Phase separation and molecular ordering of the prion-like domain of the thermosensory protein EARLY FLOWERING 3. *bioRxiv* 2023.03.12.532276 (2023) doi:10.1101/2023.03.12.532276.

64. Zhou, M. *et al.* Phase-separated condensate-aided enrichment of biomolecular interactions for high-throughput drug screening in test tubes. *J. Biol. Chem.* **295**, 11420–11434 (2020).
65. Banani, S. F. *et al.* Compositional Control of Phase-Separated Cellular Bodies. *Cell* **166**, 651–663 (2016).
66. Pei, G., Zhou, M., Xu, W., Wang, J. & Li, P. Phase Separation-Based Biochemical Assays for Biomolecular Interactions. *Methods Mol. Biol.* **2563**, 225–236 (2023).
67. Wei, M.-T. *et al.* Nucleated transcriptional condensates amplify gene expression. *Nat. Cell Biol.* **22**, 1187–1196 (2020).
68. Lyons, H. *et al.* Functional partitioning of transcriptional regulators by patterned charge blocks. *Cell* **186**, 327-345.e28 (2023).
69. Kumamoto, T. *et al.* Foxg1 coordinates the switch from nonradially to radially migrating glutamatergic subtypes in the neocortex through spatiotemporal repression. *Cell Rep.* **3**, 931–945 (2013).
70. Lu, T. & Spruijt, E. Multiphase Complex Coacervate Droplets. *J. Am. Chem. Soc.* **142**, 2905–2914 (2020).
71. Feric, M. *et al.* Coexisting liquid phases underlie nucleolar subcompartments. *Cell* **165**, 1686–1697 (2016).
72. Patel, S. S. & Rexach, M. F. Discovering novel interactions at the nuclear pore complex using bead halo: a rapid method for detecting molecular interactions of high and low affinity at equilibrium. *Mol. Cell. Proteomics* **7**, 121–131 (2008).
73. Tompa, P. & Fuxreiter, M. Fuzzy complexes: polymorphism and structural disorder in protein-protein interactions. *Trends Biochem. Sci.* **33**, 2–8 (2008).
74. Mitrea, D. M. *et al.* Self-interaction of NPM1 modulates multiple mechanisms of liquid–liquid phase separation. *Nat. Commun.* **9**, 842 (2018).
75. Ho, P. J., Lloyd, S. M. & Bao, X. Unwinding chromatin at the right places: how BAF is targeted to specific genomic locations during development. *Development* **146**, (2019).
76. Hodges, C., Kirkland, J. G. & Crabtree, G. R. The Many Roles of BAF (mSWI/SNF) and PBAF Complexes in Cancer. *Cold Spring Harb. Perspect. Med.* **6**, (2016).
77. Khavari, P. A., Peterson, C. L., Tamkun, J. W., Mendel, D. B. & Crabtree, G. R. BRG1 contains a conserved domain of the SWI2/SNF2 family necessary for normal mitotic growth and transcription. *Nature* **366**, 170–174 (1993).
78. Wang, W. *et al.* Purification and biochemical heterogeneity of the mammalian SWI-SNF complex. *EMBO J.* **15**, 5370–5382 (1996).
79. Lewis, A. K. *et al.* Oxidation increases the strength of the methionine-aromatic interaction. *Nat. Chem. Biol.* **12**, 860–866 (2016).
80. Reid, K. S. C., Lindley, P. F. & Thornton, J. M. Sulphur-aromatic interactions in proteins. *FEBS Lett.* **190**, 209–213 (1985).
81. Flores-Solis, D. *et al.* Driving forces behind phase separation of the carboxy-terminal domain of RNA polymerase II. *Nat. Commun.* **14**, 5979 (2023).
82. Zondlo, N. J. Aromatic-proline interactions: electronically tunable CH/π interactions. *Acc. Chem. Res.* **46**, 1039–1049 (2013).
83. Gallivan, J. P. & Dougherty, D. A. Cation-pi interactions in structural biology. *Proc. Natl. Acad. Sci. U. S. A.* **96**, 9459–9464 (1999).
84. Brahma, S. & Henikoff, S. RNA Polymerase II, the BAF remodeler and transcription factors synergize to evict nucleosomes. *bioRxivorg* (2023) doi:10.1101/2023.01.22.525083.
85. Patil, A. *et al.* A disordered region controls cBAF activity via condensation and partner recruitment. *Cell* (2023) doi:10.1016/j.cell.2023.08.032.
86. Thomsen, C., Grundevik, P., Elias, P., Ståhlberg, A. & Aman, P. A conserved N-terminal motif is required for complex formation between FUS, EWSR1, TAF15 and their oncogenic fusion proteins. *FASEB J.* **27**, 4965–4974 (2013).

87. Owen, I. *et al.* The oncogenic transcription factor FUS-CHOP can undergo nuclear liquid-liquid phase separation. *J. Cell Sci.* **134**, (2021).
88. Thelin-Järnum, S., Göransson, M., Burguete, A. S., Olofsson, A. & Aman, P. The myxoid liposarcoma specific TLS-CHOP fusion protein localizes to nuclear structures distinct from PML nuclear bodies. *Int. J. Cancer* **97**, 446–450 (2002).
89. Erdel, F. & Rippe, K. Formation of Chromatin Subcompartments by Phase Separation. *Biophys. J.* **114**, 2262–2270 (2018).